A Measurement of The Isolated Direct Photon Cross Section at 630 GeV

Michael Strauss, Matthew Price
University of Oklahoma, Norman, OK

DØ NOTE # 3699
August 2, 2000
Preliminary Version 1.7

Abstract

The inclusive cross section for isolated photons at $\sqrt{s} = 630$ GeV/c^2 (Run 1C) is measured for the central ($|\eta| < 0.9$) and forward ($1.6 < |\eta| < 2.5$) rapidity regions. We compare the result with next to leading order QCD predictions using CTEQ parton distribution functions.

1 Introduction

The present analysis is developed along the lines of the published Run 1A/1B cross section data [1], described in greater detail in a DØ note by S. Linn [2]. Other techniques are from previous isolated photon analysis at 1800 GeV/c^2 [3, 4, 5] and at 630 GeV/c^2 [6, 7]. This note supersedes and expands on the previous 630 GeV/c^2 analyses. The differential cross section for the process $p\overline{p} \rightarrow \gamma + X$ can be written as

$$\frac{d^2\sigma}{dE_T d\eta} = \frac{N\mathcal{P}}{L\Delta\eta\Delta E_T A\epsilon_s\epsilon_d\epsilon_t} \tag{1}$$

where N is the number of photon candidates (one or two per event), $\mathcal{P}$ is the photon purity (the fraction of direct photons in the sample), L is the integrated luminosity, $\Delta\eta$ and ΔE_T are the bin sizes in pseudorapidity and E_T, A is the geometric acceptance, ϵ_s is the efficiency of the selection criteria, ϵ_d is the efficiency of the charged track cut, and ϵ_t is the efficiency of the trigger.

Previous measurements of the isolated single photon cross section at collider energies by UA2 and CDF showed a discrepancy between the theory and the data, particularly in the low E_T regions as shown in Fig. 1 [8, 9]. The CDF data has never been published.

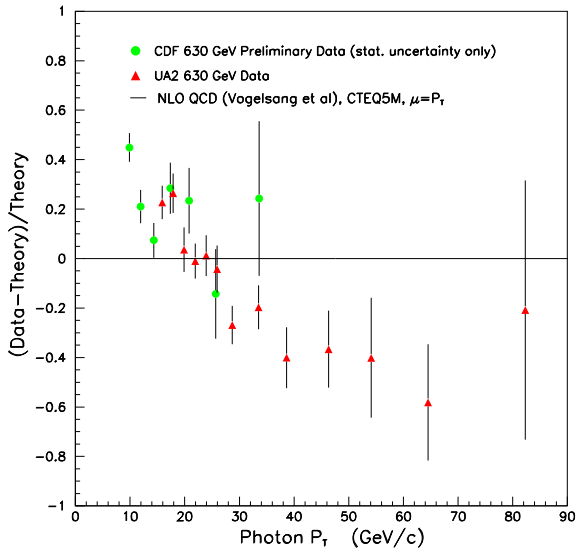

Figure 1: Production of direct photons at 630 GeV from UA2 and CDF. The data is normalized to CTEQ5 as implemented by Vogelsang.

2 Data and Monte Carlo Sample

2.1 The Direct Photon Data Set

The data in this analysis were taken at 630 GeV during the last part of Run 1C, with three dedicated isolated photon triggers, as summarized in Table 1. The respective luminosities, number of events successfully reconstructed, and events used in the analysis after all selection criteria, is also shown. The uncertainty on the luminosity is 5%.

2.2 Monte Carlo Sample

The analysis depends heavily on the Monte Carlo to determine efficiencies and background from neutral mesons. The MC sample, generated in the

L1 Trigger	L2 Filter	Thresh. (GeV)	$\int L\,dt$ (nb^{-1})	Events	Events Used
em_1_2_lnr	gam_4_iso5	4.5	2.021	52771	1890
em_1_3_lnr	gam_8_iso3	8	17.22	20597	1169
em_1_7_lnr	gam_14_iso	14	520.5	24362	3161

Table 1: 630 GeV isolated photon triggers

Florida State University farm, consists of full PYTHIA photon and electromagnetic jet events generated at $\sqrt{s} = 1.8$ TeV, with zero bias events superimposed. To minimize computing time, most of these events had only the particles in a cone of $R = 0.7$ around each photon or jet simulated through DØGEANT, using plate level calorimeter geometry. These events are used to estimate the photon purity, $\mathcal{P}$ (see Section 5). A smaller number of events had the entire event simulated in the detector and are used for determining selection efficiencies, (Section 3.4).

In an attempt to maximize MC statistics within the allotted cpu budget, about ten different zero bias events were overlayed for the same PYTHIA event. Although the events in this MC sample are clearly not independent, studies have indicated only a moderate degree of correlation [10]. This point is addressed further in Appendix A. The number of available MC events is summarized in Tables 2 and 3 for six E_T ranges, in the central and forward regions, respectively

E_T Range	*Before All Cuts*			*After All Cuts*		
	Data	MC γ	MC Jets	Data	MC γ	MC Jets
6 – 8	6681	12746	32061	908	6262	7144
8 – 13	8817	26199	42169	742	14862	9495
13 – 18	5719	15731	22566	967	10015	6038
18 – 23	3091	17694	15017	865	12188	4559
23 – 33	1516	19423	15977	377	13074	4908
>33	432	41442	24578	67	29542	8078

Table 2: Number of Data and MC events in central rapidity region as a function of E_T, in bins used for calculating photon purity.

E_T Range	*Before All Cuts*			*After All Cuts*		
	Data	**MC γ**	**MC Jets**	**Data**	**MC γ**	**MC Jets**
6 – 8	4614	2590	14081	599	1625	3674
8 – 11	5734	13903	17244	313	9188	3880
11 – 15	3036	16830	15914	238	11255	3590
15 – 20	5246	16293	18104	821	11239	4187
20 – 26	1361	17873	12162	256	12501	3129
>26	334	36490	27848	67	25544	7389

Table 3: Number of Data and MC events in forward rapidity region as a function of E_T, in bins used for calculating photon purity.

The ability of the MC to model the data was previously tested by comparing 40 GeV simulated electrons with electron candidates from $W \rightarrow e\nu$ Run 1B events [5]. As there are very few W events for the 630 GeV sample, this comparison could not be performed with the runs corresponding to the data used for the present analysis. A comparison of the effect of selections on data and fully simulated Monte Carlo photons demonstrated that within statistical accuracy, the two samples were affected in a similar manner.

Because the Monte Carlo data set was generated at $\sqrt{s} = 1.8$ TeV a comparison of the distribution of the selection variables between the Monte Carlo and the data is made to confirm that the Monte Carlo adequately described the 630 GeV data. The details of this comparison are covered in Appendix B.

2.3 Event Selection

The selections used on the MC sample (where applicable) and data are:

- $|\eta| < 0.9$ ($1.6 < |\eta| < 2.5$) for the central (forward) region.
- $|\eta^{det}| < 9$ ($16 < |\eta^{det}| < 25$) for the central (forward) region.
- $|Z_{vertex}| < 50\,\mathrm{cm}$
- For the central region, $0.1 < \mathrm{mod}(16\phi/\pi) < 0.9$.
- No track in the CDC pointing to the EM cluster within $\delta\phi \times \delta\theta$ of 0.2 $\times$ 0.2

- $\frac{EM\,E^{R\leq 0.2}}{Total\,E^{R\leq 0.2}} > 0.96$
- Isolation cut: $E_T^{R\leq 0.4} - E_T^{R\leq 0.2} < 2.0\,\mathrm{GeV}$.
- H-matrix $\chi^2 < 150$

The first four cuts are labeled acceptance cuts because they constrain the candidate photon and its surrounding cone of isolation to the geometric regions where the detector is well understood. The last three, collectively named selection criteria, are tuned to selectively reject QCD jet contamination in the candidate sample.

3 Calculation of efficiencies

3.1 Trigger Efficiency

The trigger efficiency for the high and medium energy triggers is determined from the data, while the low-energy trigger efficiency is determined using Monte Carlo events. The inability to determine the low-energy trigger efficiency with data is one of the weaknesses of this analysis. The sensitivity of the cross section to the correct trigger efficiency from Run 1A is shown in Fig. 2. The isolation requirements and trigger efficiency correction are different for Run 1A at 1800 GeV and Run 1C at 630 GeV, so the correction used in Run 1A is not applicable in this analysis. To minimize the effect of the uncertainty in the low-energy triggers, we chose not to use the lowest threshold data in the final cross section.

This analysis relies on a common method to determine the high energy (14 GeV) and medium energy (8.0 GeV) trigger efficiencies, and on a complementary method to check the high energy trigger efficiency. The results from the two methods are averaged together and their difference is taken as a measure of the systematic uncertainty.

The common method used by the medium and high energy triggers simply takes the ratio of the number of 14 GeV (8.0 GeV) triggers divided by the number of 8.0 GeV (4.5 GeV) triggers, with both triggers scaled by the appropriate luminosity factors taken from the run database. The trigger turn on ratios are shown in Fig. 3 and Fig. 4 for the CC and EC, respectively. We estimate the systematic uncertainties in the medium energy regime from those determined in the high energy regime.

The alternative method for finding the high energy efficiency uses all events that fire the medium energy trigger as tagged events. The fraction

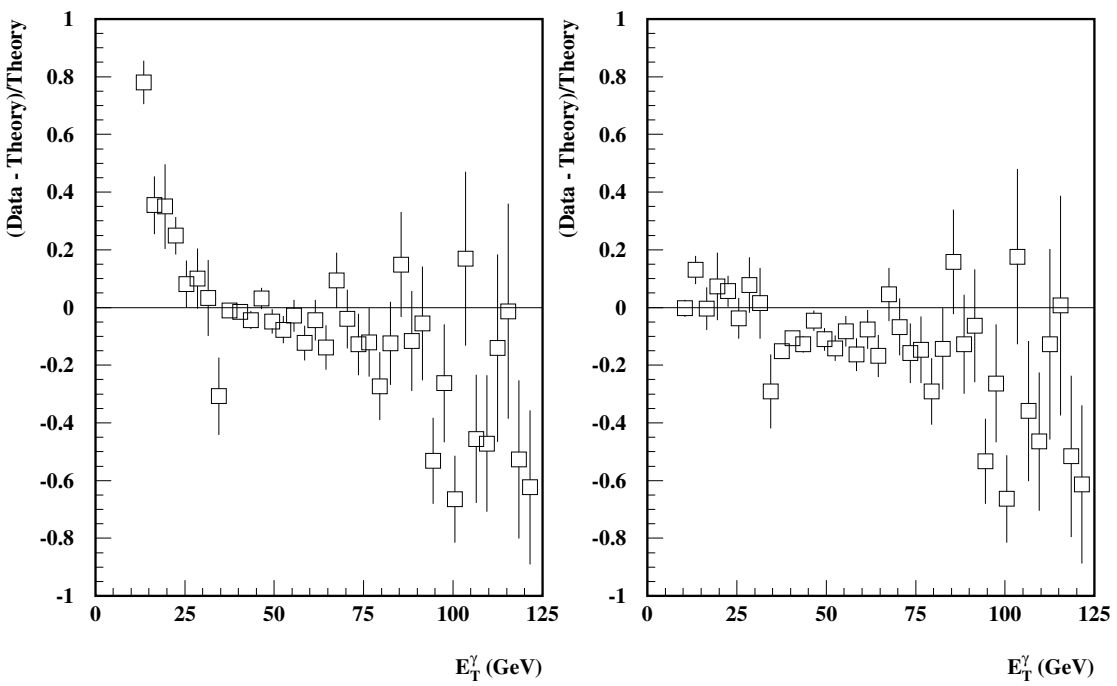

Figure 2: Effect of trigger efficiency on Run 1A data. *Left*: Published result for the CC region. *Right*: Same data, but without the correction for trigger efficiency.

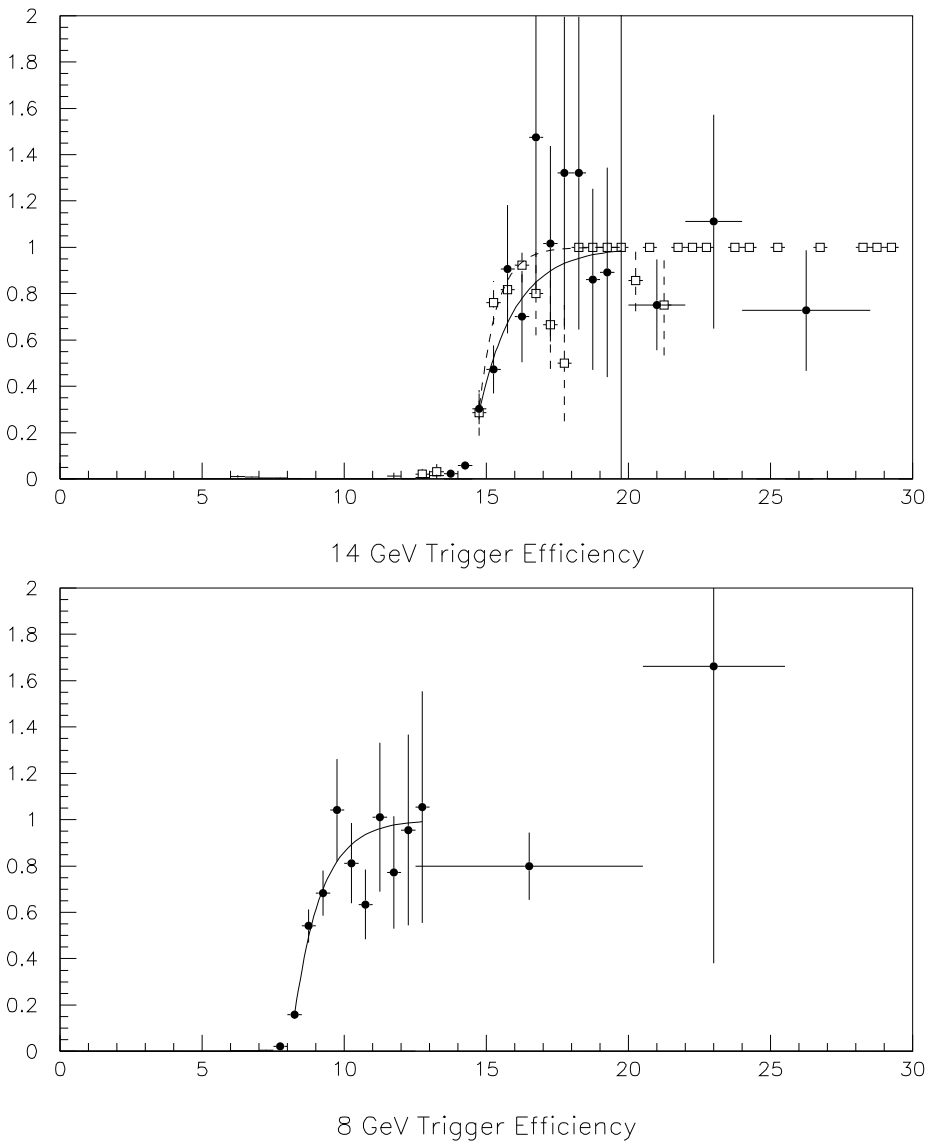

Figure 3: Trigger efficiency for the central region. The black circles (and solid line) show the efficiency determined from the luminosity corrected data described in the text, and the open squares (and dashed line) show the efficiency determined from the direct method that is only applicable to the high energy trigger.

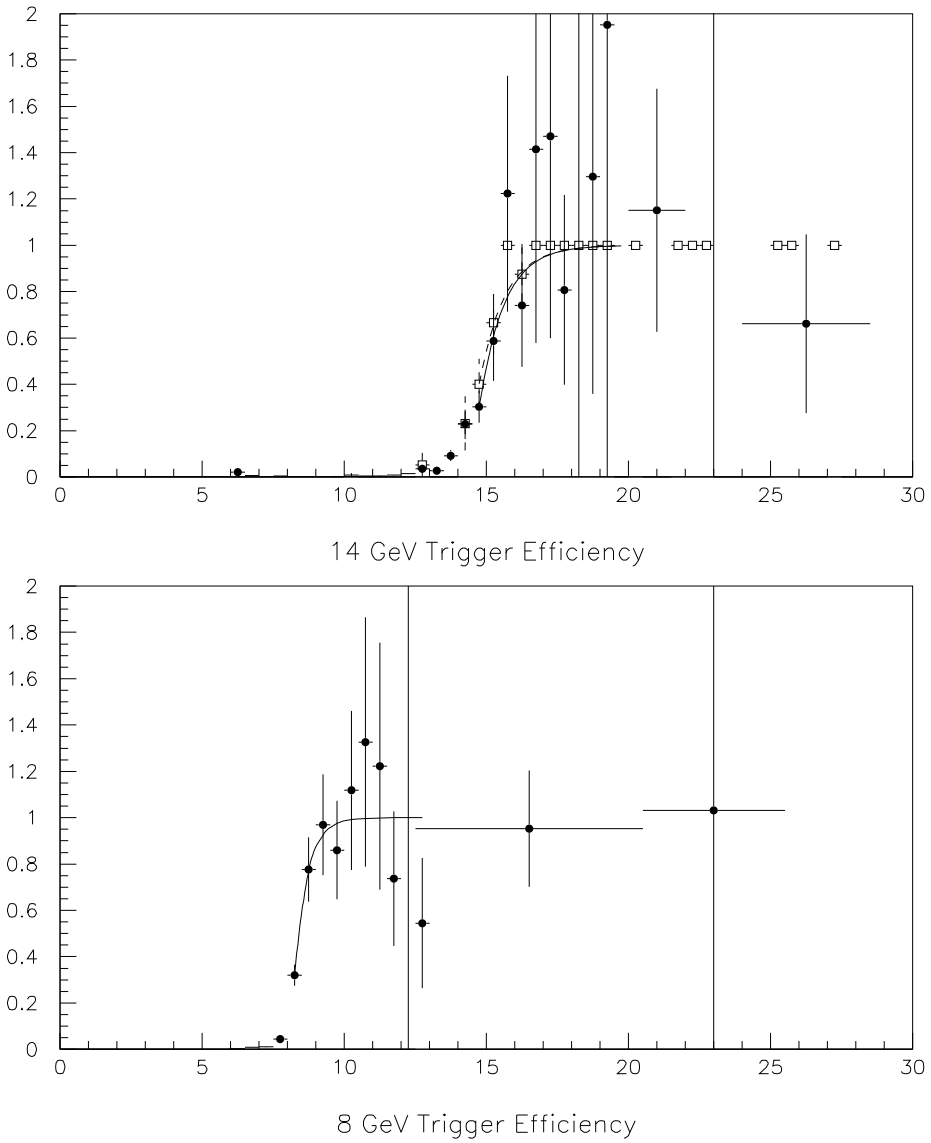

Figure 4: Trigger efficiency for the forward region. The black circles (and solid line) show the efficiency determined from the luminosity corrected data described in the text, and the open squares (and dashed line) show the efficiency determined from the direct method only applicable to the high energy trigger.

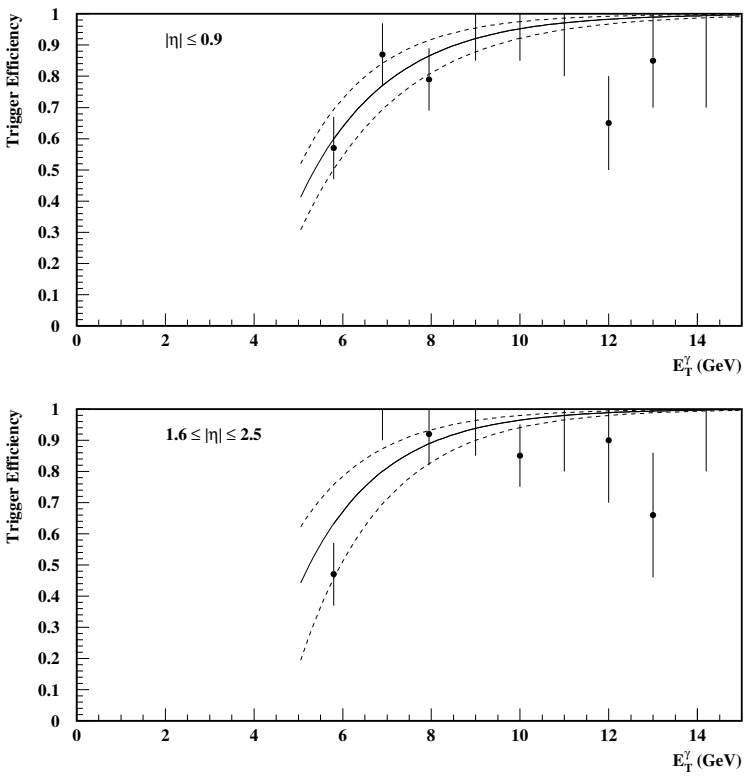

Figure 5: Low energy trigger efficiencies for the central and forward regions.

of these tagged events that also fire the high trigger defines the efficiency. This alternative method can only be used for the 14.0 GeV trigger because it requires that all tagged events have the potential of firing the higher energy trigger; a criteria that is only satisfied if the higher energy trigger is not prescaled. This alternative method is also shown in Fig. 3 and Fig. 4. Note that for the EC, the two methods of determining the high energy trigger efficiency give almost identical results, while for the CC, the fit results differ by 1.3σ.

The points are fitted with a functional form

$$\epsilon_t = 1 - e^{(b-E_T)/a} \tag{2}$$

where a and b are free parameters, with b approximately equal to the trigger threshold energy.

It is not possible to determine the low energy efficiency from the data, so instead we use results of a MC study carried on by A. Schaffer in 1995 [11], with events generated for the Run 1A analysis, both for the central and forward rapidity regions.

Threshold	**Region**	**a**	**b**
4.5 GeV	CC	1.97 ± 0.32	4.5
8.0 GeV	CC	$0.98 \pm 0.16 \pm 0.08$	$8.08 \pm 0.04 \pm 0.04$
14.0 GeV	CC	$0.96 \pm 0.33 \pm 0.32$	$14.40 \pm 0.18 \pm 0.10$
4.5 GeV	EC	1.80 ± 0.32	4.5
8.0 GeV	EC	$0.45 \pm 0.14 \pm 0.07$	$8.07 \pm 0.05 \pm 0.04$
14.0 GeV	EC	$0.89 \pm 0.43 \pm 0.05$	$14.36 \pm 0.25 \pm 0.08$

Table 4: Trigger efficiency used for this analysis fit to the functional form $\epsilon_t = 1 - e^{(b-E_T)/a}$. The uncertainty shown for the 4.5 GeV trigger is both statistical and systematic, while the statistical and systematic uncertainties for the 8 and 14 GeV trigger are shown separately.

The low energy trigger efficiency is shown in Fig. 5. The points are fitted with the functional form in Eq. 2 with $a = 1.97 \pm 0.32$ (1.80 ± 0.30) in the central (forward) region and b set to the threshold energy of 4.5 GeV. The error bands are enlarged to account for other possible functional dependences. The trigger efficiencies used in this analysis are summarized in Table 4. The uncertainty in the determination of the trigger efficiency below 7 GeV is one of the very large systematic uncertainties that affect the low-E_T region.

In addition, there is a large background fraction which causes a very large percent uncertainty in the determination of the purity in the low-E_T region (Section 5). Also, the selection efficiency is not well determined below about 7 GeV (section 3.4). Because of these three problems, we choose 7 GeV as the minimum E_T for quoting a cross section.

To check that the various triggers are consistent with each other, we plot the number of events satisfying the selections divided by the luminosity, as a function of E_T for the central and forward regions in Fig. 6. In Fig. 7 the normalized difference is plotted. As expected if there are no inconsistencies between triggers, each ratio moves from a value of 1 to a value of zero at some energy above the trigger threshold. Because the normalized difference goes to zero about 2 GeV above the trigger threshold, we use events that fire the 8 (14) GeV trigger if they have $E_T > 10$ (16) GeV. With these thresholds, no systematic problems in the trigger are apparent.

3.2 Acceptance

The acceptance A takes into account the events lost due to the the various geometric selection criteria which eliminates section boundaries in the CC (20% of the ϕ region is eliminated), keeps only events coming from near $Z_{vertex} = 0$, and rejects events in certain regions of η^{det}.

The acceptance in Z_{vertex} is estimated by taking the ratio of events with and without the Z_{vertex} requirement and found to be .848 (.846) for the CC (EC). The vertex distribution is shown in Fig. 8 fitted to a Gaussian function.

The acceptance in η^{det} is taken from the Run 1B analysis, and is 0.917 ± 0.007 (0.930 ± 0.007) in the central (forward) region [5]. It was calculated from a MC simulation, using an η distribution modeled by Owens et al. [12]. The systematic uncertainty corresponds to the difference obtained for a flat distribution in physics η and the above distribution. This systematic uncertainty is large enough to encompass any minor differences in shape between the 1800 and 630 GeV distributions.

Combining the three separate sources of loss, the total acceptance is $A = 0.622 \pm 0.007$ (0.787 ± 0.007) in the central (forward) pseudorapidity region.

3.3 Charged Track Efficiency

The presence of a charged track near a shower distinguishes electrons from photons. By removing EM objects with an associated charged track extrapolated from the wire chambers, contamination of the photon signal by electrons is greatly reduced. However, this can lead to rejection of signal if a

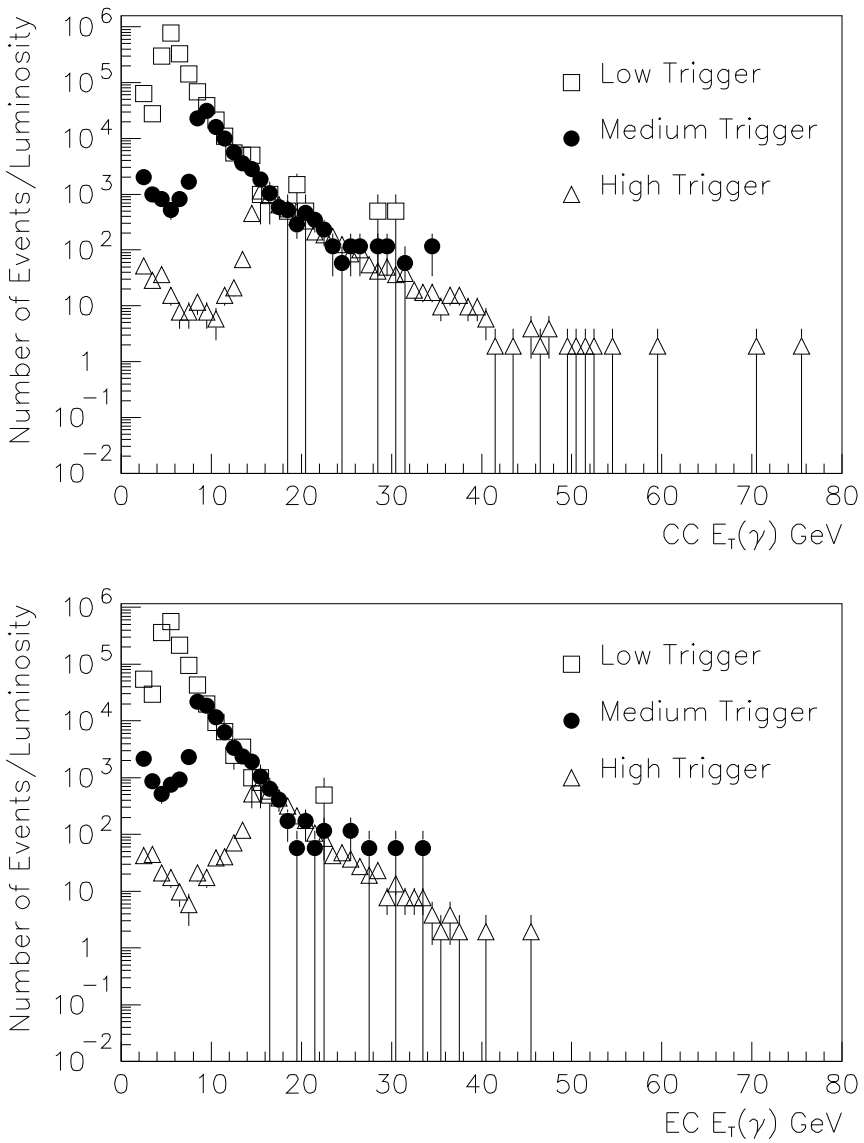

Figure 6: Luminosity-corrected yields for the central and forward region as a function of E_T.

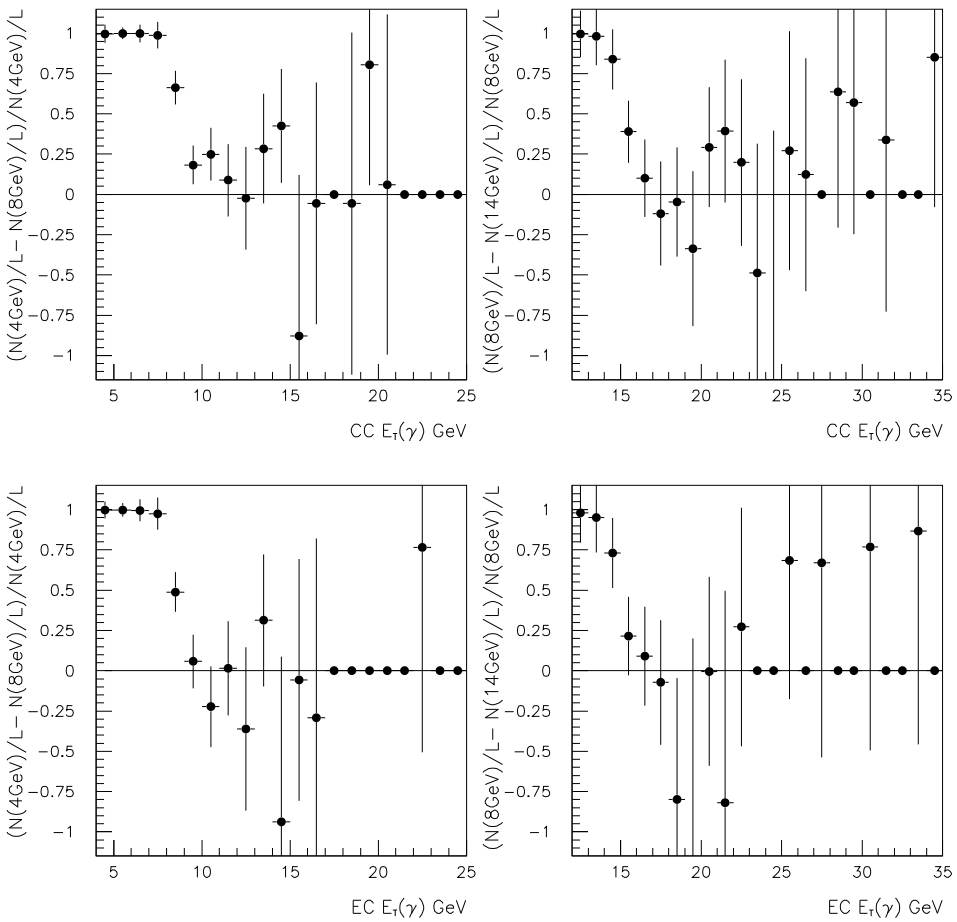

Figure 7: Normalized luminosity-corrected yields for the central and forward region as a function of E_T The analysis described in this note requires a threshold of 10 (16) GeV for events that fired the 8 (14) GeV trigger .

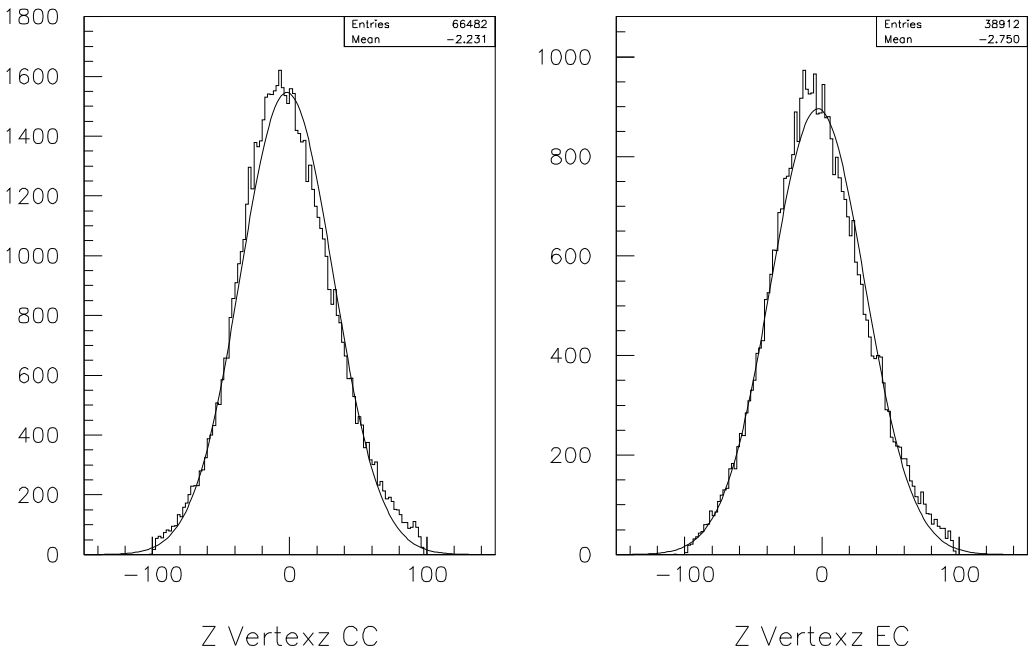

Figure 8: Vertex distribution of isolated photon events

direct photon has converted or has an unrelated overlapping charged track. The effect is more important in the EC due to the higher track density and the larger amount of material for the photon to convert.

The overall tracking efficiency is parameterized as

$$\epsilon_d = (1 - pt)(1 - \psi)$$

where p is the probability that a photon will convert before the tracking chambers, t is the probability that a track in the detector will be reconstructed, and ψ is the probability that a reconstructed track from the underlying event will be found in the tracking road of a good photon.

The parameter p has been determined previously to be 0.095 ± 0.010 (0.386 ± 0.041) for the CC (EC)[4]. To determine the other parameters, we use a sample of $Z^0 \to e^+e^-$ events from Run 1C (at 1.8 TeV) because the number of Z^0 events at 630 GeV was found insufficient. Z^0 events with no jets in the event are chosen to avoid electrons that may have overlapped a jet, and to ensure a topology similar to that of photon events where any jets are generally in the opposite hemisphere from the photon. Both EM clusters are also required to have a reconstructed E_T above 25 GeV.

To determine t, each electron from the Z^0 decay is checked against the

following requirements:

- $\eta < 0.9$
- At least one track in the road $\delta\phi \times \delta\theta = 0.2 \times 0.2$.
- Track match significance $\sigma_t < 5$ (10) in the CC (EC).
- EM fraction $> 95\%$
- Isolation fraction $< 20\%$
- Hmatrix $\chi^2 < 100$.

An EM shower passing these requirements is tagged as a good electron, and the other electron from Z^0 decay is considered unbiased and usable for determining the tracking efficiency. Photon selections, except the tracking cut, are applied to the unbiased sample and any candidate that passes these cuts is checked for $\sigma_t < 5$ (10) in the CC (EC). Invariant mass distributions are calculated for all candidates passing the photon selections, both with and without the tracking criteria. The tracking efficiency is determined by calculating how many electrons from $Z^0 \rightarrow e^+e^-$ events pass the tracking requirement. The number of events in the Z^0 signal region (N_S) is determined from events having an invariant mass between 86 and 96 GeV/c^2. The background is defined in two regions on either side of the Z^0 peak from 61 to 71 GeV/c^2 and from 111-121 GeV/c^2, with the number of background events (N_B) being half of the total number in these two regions. Events with and without tracks in the CC and EC are shown in Fig. 9. The tracking efficiency is given by

$$t = \frac{N_{TS} - N_{TB}}{N_S - N_B}$$

where the subscript T indicates the number of events with associated tracks. The tracking efficiency is estimated as $t = .769 \pm .024 \pm .017$ ($.683 \pm .042 \pm .002$) in the CC (EC), where the first error is statistical and the second systematic, the latter estimated by the difference in efficiency with and without background subtraction.

The track overlap probability, ψ, is obtained using the same method described above for determining t, but with an additional track in the road pointing to the EM cluster. The estimated track overlap probability is $\psi = .074 \pm .014 \pm .008$ ($.195 \pm .033 \pm .044$) in the CC (EC), where the first error is statistical and the second is systematic. The systematic uncertainty is

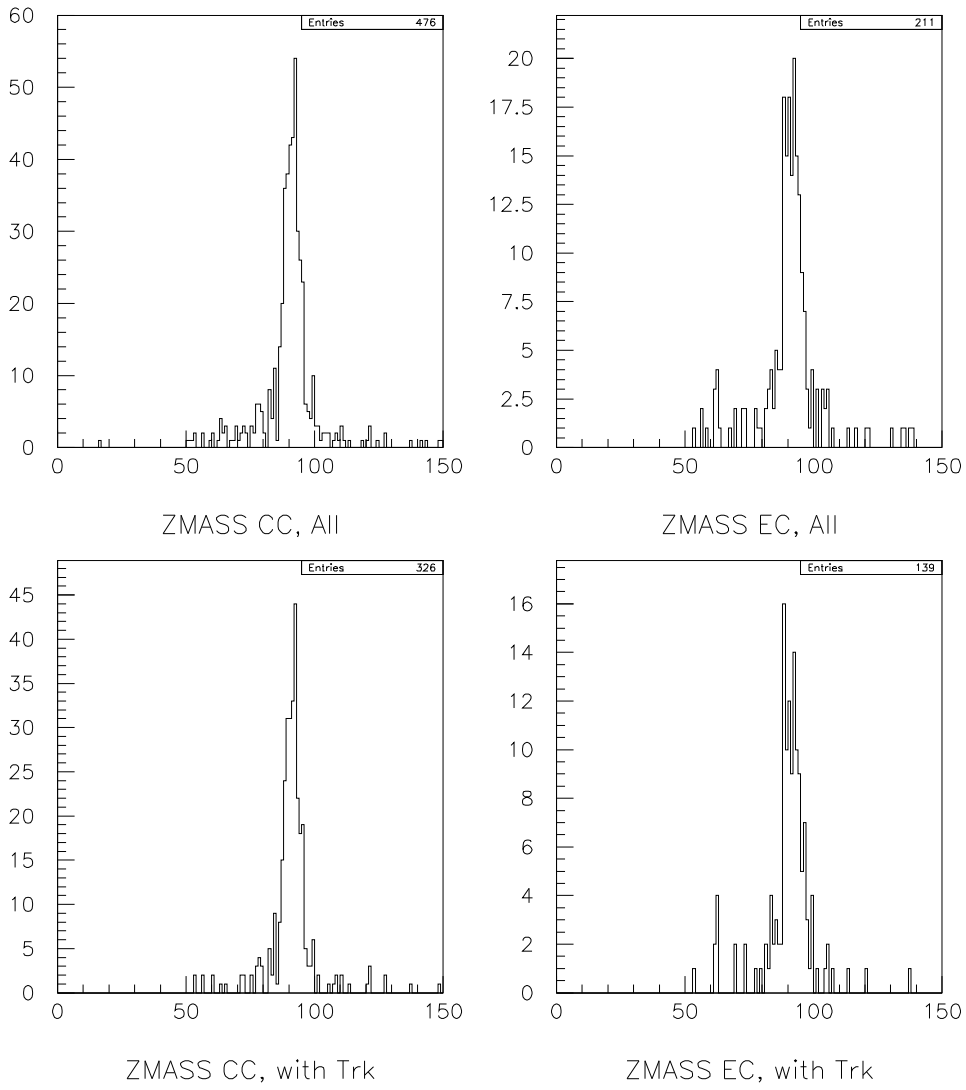

Figure 9: Invariant mass peaks for events with an unbiased EM cluster passing photon selections and for the same events also passing electron tracking requirements in the CC and EC.

estimated from a comparison of two different methods used in the Run 1A analysis to determine ψ. One of the methods is the same as used in this analysis, and the other uses very clean photons and any tracks in the road pointing to the cluster [5]. The percent difference between the two methods for the Run 1A analysis is used as the systematic uncertainty in this analysis.

Combining the values for p, t, and ψ, the total tracking efficiency is found to be $\epsilon_d = 0.858 \pm 0.018$ (0.593 ± 0.079) in the central (forward) region. The Monte Carlo tracking efficiency is adjusted to match these values.

3.4 Selections

The selections listed in Section 2.3 are applied to remove most of the multi-particle background. The isolation, EM fraction, and H-matrix χ^2 cuts select EM objects consistent with being single particle showers.

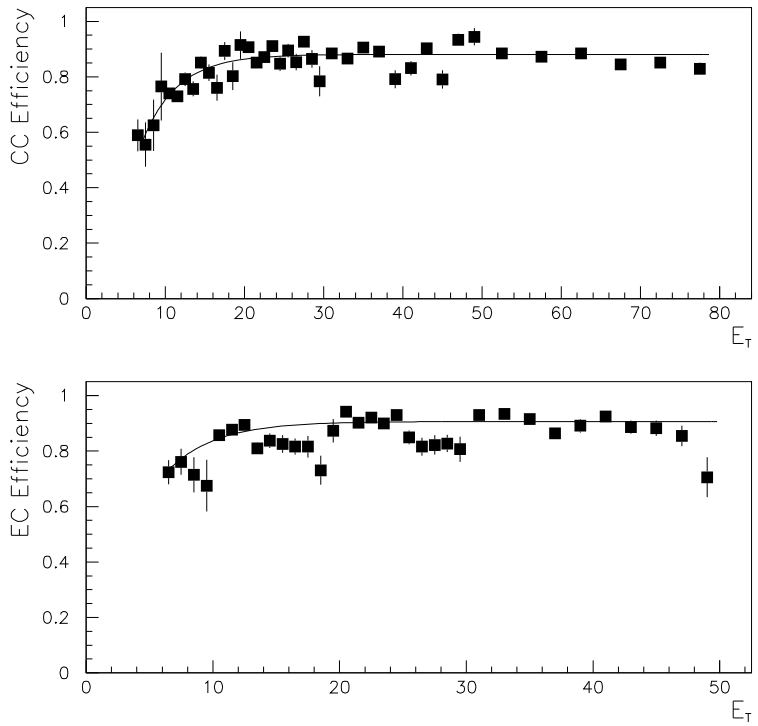

Figure 10: Selection efficiencies for the central and forward η regions.

The selection efficiencies, shown in Fig. 10, are estimated using Monte

Carlo photon events that are fully simulated in the entire DØ detector. Only photons with reconstructed energies that are in the same E_T regions as the generated photons are used for the selection efficiency determination, (e.g. photons generated between 20 and 30 GeV, but reconstructed with an energy of 18 GeV would not be used). This criteria is necessary because the photons with reconstructed energy lower than the generated energy are those that are poorly reconstructed and give much lower selection efficiency. Because the Monte Carlo is generated in different E_T regions, there are a large number of photons generated in a higher E_T region (say 20-30 GeV) which are reconstructed in a lower E_T region, (10-20 GeV in this case) just as the cross section, and number of events, is diminishing in the lower region. However, the data is a steeply falling function of E_T and does not exhibit artificial boundaries where a large number of higher energy photons are created and could contaminate a lower E_T region. The "Filter" criteria, (see Section 6) eliminates this potential problem across trigger boundaries.

The the selection efficiency is fitted as a function of E_T with the functional form

$$\epsilon_t = c - e^{(b-E_T)/a}. \tag{3}$$

Fit results for the CC (EC) give $a = 4.43 \pm 0.76$ (3.81 ± 1.14), $b = 1.95 \pm 1.47$ (-0.145 ± 2.810), and $c = 0.881 \pm 0.004$ (0.907 ± 0.005). A detailed discussion of how the simulation of efficiencies was verified at 40 GeV, using electrons from W decay, can be found in References [4, 5].

4 Monte Carlo Energy Scale

For the forward region, the MC distributions have an offset in $\log(1+\log(1+E_1))$ with respect to the data, which has been shown to be due to incorrect sampling fraction used in the simulation [4, 5]. The discriminant $\log(1+\log(1+E_1))$ is used to determine the purity of the photon sample. (See Section 5.1.)

We choose to parameterize this offset using the same method as the Run 1A/1B analysis. [2] We assume that the parameterization is of the form $E_1^{MC} = \alpha + \beta E_1$ where α and β are determined from the data. The value of β is eliminated using the $W \to e\nu$ sample so that $\beta = (E_1^{MC}(W) - \alpha)/E_1(W)$. The value of α is extracted by fitting the purity $\mathcal{P}$ (see Section 5.1)) for various values of α and choosing the value of α with the lowest global χ^2, the sum of the χ^2 value from the fit to each energy bin. The global χ^2 as a function of the value of α is plotted in Fig. 11. The minimum is found at a value of $\alpha = 62 \pm 2$ MeV.

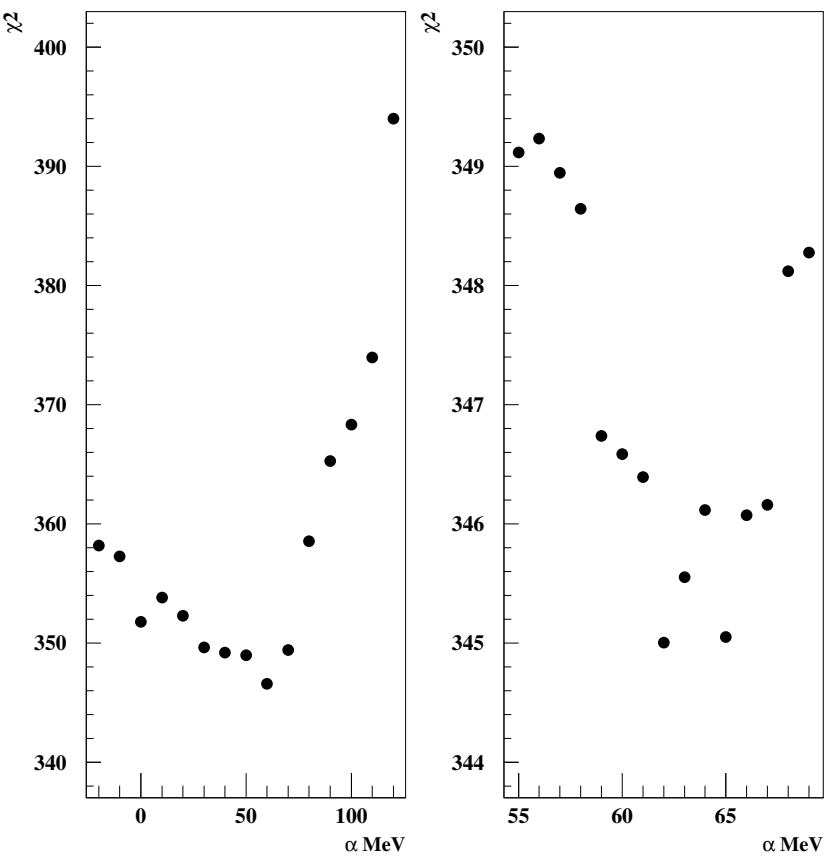

Figure 11: χ^2 of the Purity fit in the EC as a function of the non-linear energy shift α.

5 Photon Purity

5.1 Purity Determination

The isolated direct photon sample is contaminated with a background arising from jets that have fluctuated into isolated EM objects. It consists mainly of single or multiple isolated π^0 and η mesons which decay into photons not resolved because of the calorimeter granularity. This background cannot be singled out on an event by event basis, and is corrected instead in each E_T region by means of an average photon fraction, or purity ($\mathcal{P}$), defined as the ratio $\mathcal{P} = \gamma/(\gamma+\text{jet})$, where γ and jet correspond to the number of direct photons and background jets that survive the selection criteria, respectively.

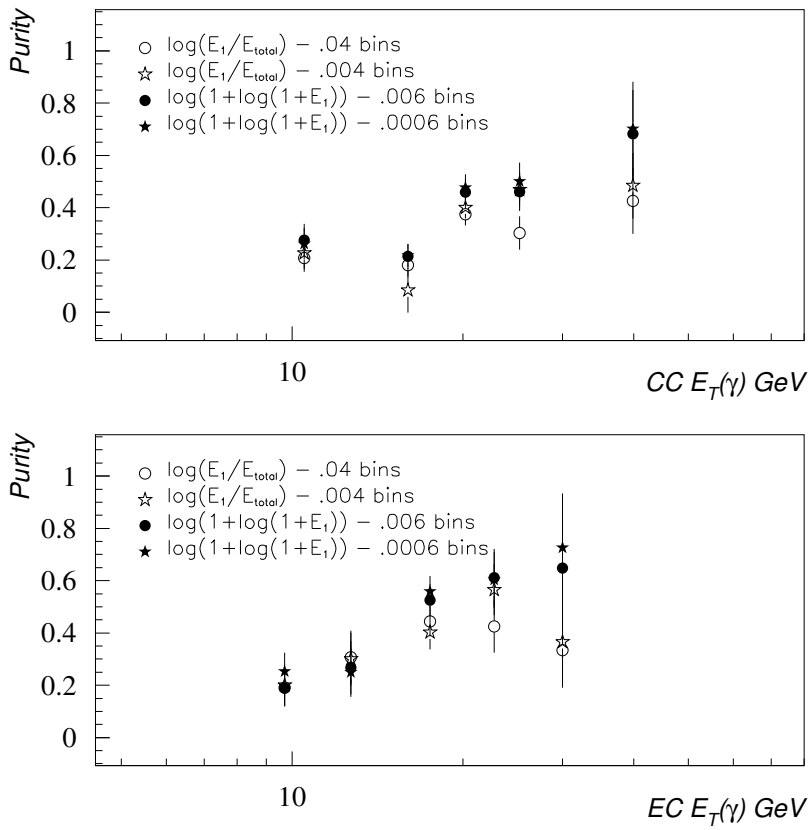

Figure 12: Photon purity using different discriminants, showing the bin size for each discriminant.

The photon purity is estimated by comparing the distributions of different observables in the data with MC predictions for photons and jets. Variables sensitive to the difference between single and multi-photon showers, and well reproduced by the MC simulation, are particularly suitable for this analysis. Following analyses in Run 1A and Run 1B, we investigate the fraction of energy deposited in the first layer of the EM calorimeter (E_1). Single photon showers are less likely to convert early, and thus deposit a smaller E_1 fraction on average. A discriminant that enhances the sensitivity to the small E_1 region where the difference between single and multi-photon events is largest must be used.

We compare two discriminants to determine the purity, $\log(E_1/E_{total})$ and $\log(1+\log(1+E_1))$, the former used in the Run 1A analysis and the latter used in the combined Run 1A/1B analysis. The results obtained from $\log(E_1/E_{total})$ are somewhat dependent on the size of the histogram bins used in the fit while the results obtained from $\log(1+\log(1+E_1))$ are much less dependent on bin size and well behaved. As a general rule, the purity determined from $\log(E_1/E_{total})$ moves closer to the value determined from $\log(1+\log(1+E_1))$ as the bin size in the first discriminant decreases. Fig. 12 shows the fitted purity for the two different discriminants and different histogram bin sizes.

Fig. 13 presents the data vs. $\log(1+\log(1+E_1))$ for the central region of rapidity with E_T bins of 6–8, 8–13, 13–18, 18–23, 23-33, and >33 GeV, together with MC contributions from photons and jets. The Monte Carlo distributions are fitted to the data using the HBOOK routine HMCMLL, which correctly incorporates statistical errors in both the data and the MC histograms. The mean photon fraction is then obtained by fitting the data to a combination of three distributions: photons, jets, and jets which contain charged tracks. The latter distribution is used as an additional parameter because the Monte Carlo sample was generated with fewer charged particles in the vicintiy of EM clusters. As with the Run 1A/1B analysis, a systematic uncertainty is assigned to the use of PYTHIA to model jets. This uncertainty is estimated by varying the multiplicity of neutral mesons in the core of the jet by $\pm 10\%$ [1].

Figure 14 presents the EC data vs. $\log(1+\log(1+E_1))$. The routine HMCMLL is used, and the purity is determined from the same fit as that used in the CC. Tables 5 and 6 give the numerical results of the fits shown in Figs. 13 and 14.

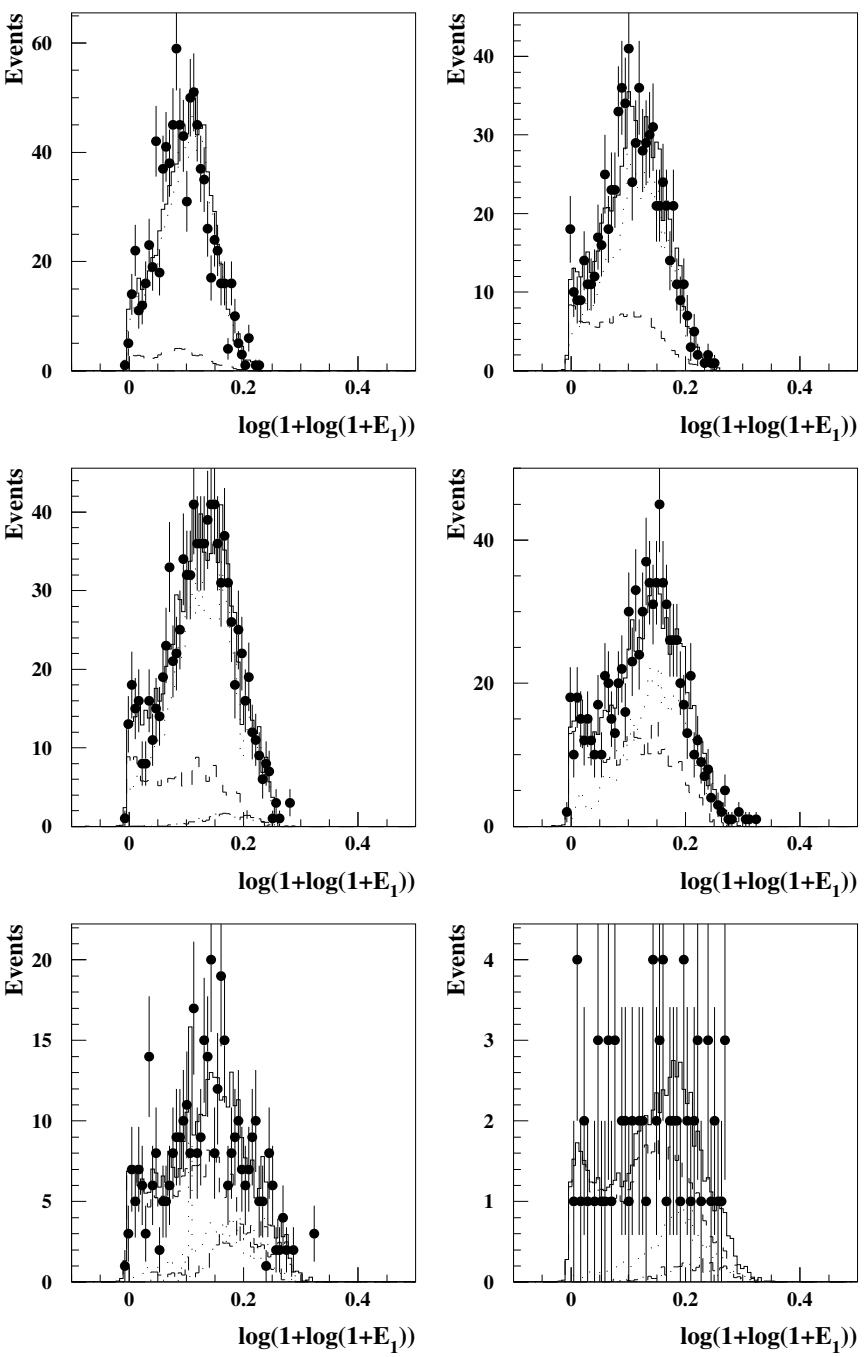

Figure 13: Distributions of $\log(1 + \log(1 + E_1))$ for the central η region in E_T bins of 6–8, 8–13, 13–18, 18–23, 23–33, and >33 GeV. The solid line is total MC fit to the data. The dashed line is the photon contribution, the dotted line is the jet background contribution, and the dash-dot line is the additional contribution from jets containing charged tracks.

E_TRange (GeV)	E_T(GeV)	HMCMLL Fit
6- 8	6.9	9.3 ± 6.8
8-13	10.5	27.6 ± 6.2
13-18	16.0	22.6 ± 5.2
18-23	20.2	45.9 ± 5.0
23-33	27.2	59.3 ± 8.1
>33	43.3	72.0 ± 20.4

Table 5: Results for photon purity in the CC.

E_TRange (GeV)	E_T(GeV)	HMCMLL Fit
8-11	9.7	30.9 ± 8.6
11-15	12.7	42.2 ± 11.3
15-20	17.5	59.5 ± 6.2
20-26	22.7	62.7 ± 10.9
>26	34.3	71.8 ± 18.1

Table 6: Results for photon purity in the EC.

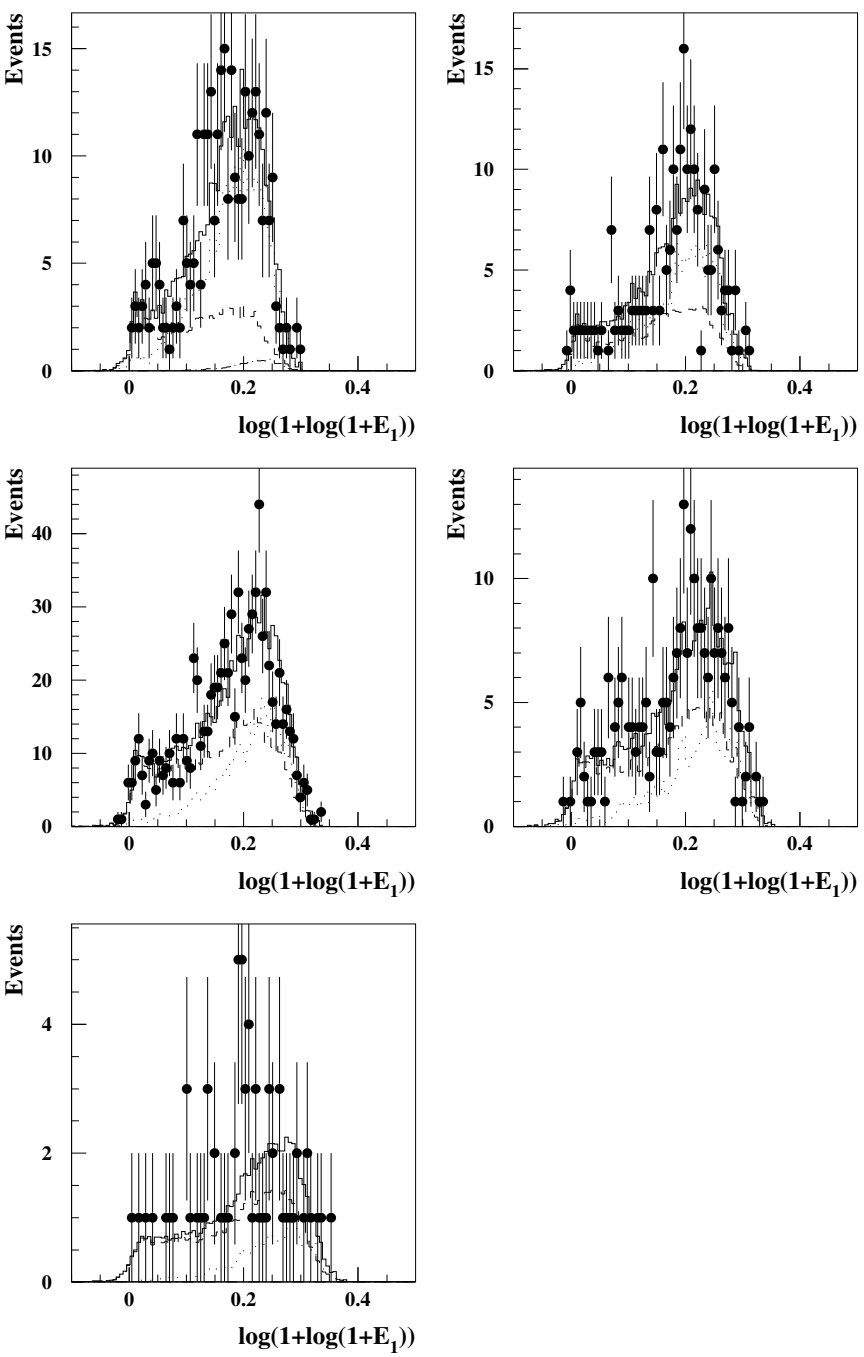

Figure 14: Distributions of $\log(1 + \log(1 + E_1))$ for the forward η region in E_T bins of 8–11, 11–15, 15–20, 20–26, and >26 GeV. The solid line is total MC fit to the data. The dashed line is the photon contribution, the dotted line is the jet background contribution, and the dash-dot line is the additional contribution from jets containing charged tracks.

5.2 E_T Dependent Fit

The photon fractions are fitted vs. E_T using a two-parameter functional form:

$$\mathcal{P}/\epsilon_s = \frac{1}{1 + a(E_T)^b}.$$

The fit, shown in Fig. 15 with its statistical uncertainty, assures that $\mathcal{P}/\epsilon_s$ is a smooth function of E_T. This functional form is chosen because it satisfies the boundary conditions of low purity at low E_T and high purity at high E_T (approaching a value of 1), and because we expect the data to be a sum of two falling cross sections (photons and jets) roughly of the form aE_T^b.

In order to estimate the uncertainty from our choice of E_T binning and fitting function, we use two alternative functions. The alternative fitting functions are

$$\mathcal{P}/\epsilon_s = 1 - e^{-(a+bE_T)},$$

and

$$\mathcal{P}/\epsilon_s = a + b \log E_T.$$

		Fitting Functions		
$\boldsymbol{E_T}$ **Bins**	Fit	$\frac{1}{1+ax^b}$	$1 - e^{-(a+bx)}$	$a + b \log x$
6-8-13-	a	291 ± 127	$-.125 \pm .085$	$-.552 \pm .293$
18-23-33	b	$-1.79 \pm .15$	$.0333 \pm .0057$	$.325 \pm .108$
6-7-10-	a	278 ± 135	$-.144 \pm .078$	$-.663 \pm .145$
16-20	b	$-1.79 \pm .16$	$.0354 \pm .0050$	$.371 \pm .051$
6-8-11-	a	81.7 ± 41.3	$-.1295 \pm .0872$	$-.416 \pm .154$
15-20-26	b	$-1.34 \pm .17$	$.0268 \pm .0056$	$.276 \pm .055$

Table 7: Fitting the Purity in the central region, using different functions and different binning with $x = E_T$.

A comparison of the fit parameters in Tables 7 and 8, and the curves in Fig. 16 indicate that the spread on all of the alternative fits is smaller or comparable to the individual errors on the data points. The fitted function is smooth and does not exhibit the statistical fluctuations inherent in the data. The systematic uncertainty is estimated by calculating the rms value of the different fits from the default choice, setting an upper limit of $\mathcal{P} = 1.0$ on each fit due to physical considerations. The complete error matrix for

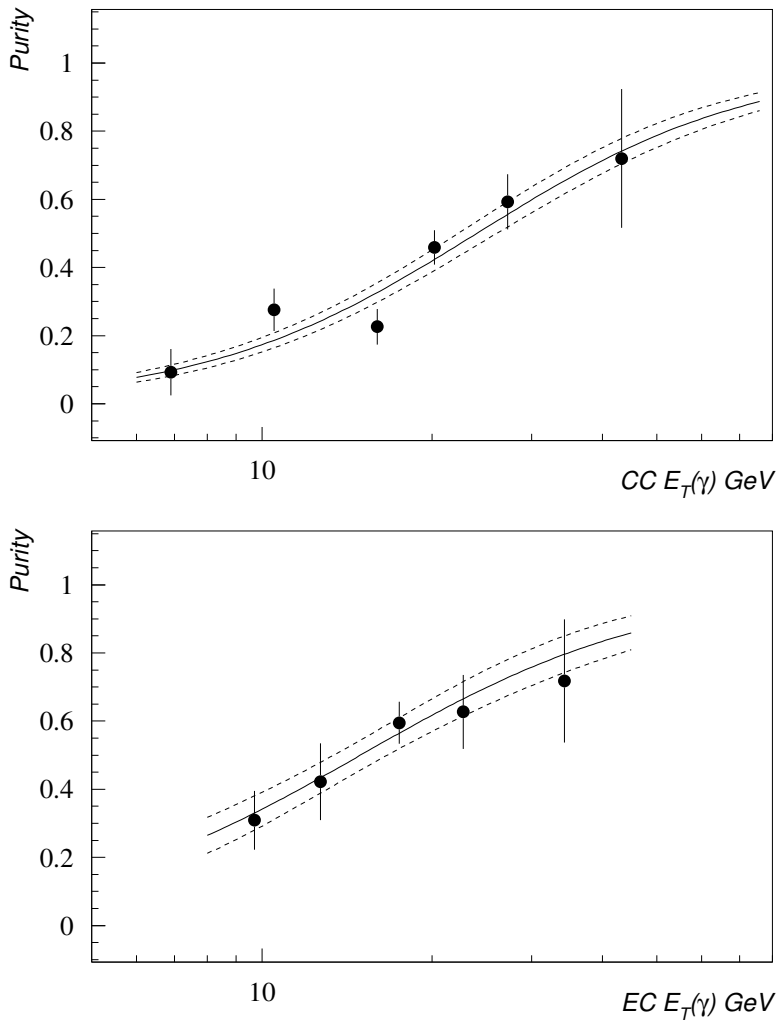

Figure 15: Photon purity for the central and forward regions. The dashed line shows the statistical uncertainty in the fit.

E_T Bins		Fitting Functions		
	Fit	$\frac{1}{1+ax^b}$	$1-e^{-(a+bx)}$	$a+b\log x$
8-13-18-23	a	234 ± 410	$-.294 \pm .297$	$-.703 \pm .350$
	b	$-2.04 \pm .64$	$.0680 \pm .0209$	$.450 \pm .125$
7-10-16-20	a	424 ± 735	$-.352 \pm .114$	$-.663 \pm .250$
	b	-2.32 ± 1.636	$.0779 \pm .0092$	$.510 \pm .090$
8-11-15-20-26	a	83.9 ± 77.2	$-.129 \pm .500$	$-.517 \pm .322$
	b	$-1.64 \pm .33$	$.0544 \pm .0344$	$.375 \pm .116$

Table 8: Fitting the Purity in the forward region, using different functions and different binning with $x = E_T$.

this systematic uncertainty is calculated using the definition of covariance, so that each element of the matrix is:

$$V_{i,j} = \frac{1}{N} \sum_k (x_k(i) - \mu(i))(x_k(j) - \mu(j))$$

where i and j are different E_T bins, $V_{i,j}$ is an element of the error matrix, the sum is over the various fitting functions, N is the number of different functions used to fit the data, and μ is the value of the default fit. The diagonal elements of this matrix is just the rms. In Fig. 17, we plot the systematic band in uncertainty determined from the rms, using all of the alternative fits and binning, as well as the default fit and its statistical error.

As a cross check of the statistical and systematic uncertainty of the E_T dependent purity fits, the same analysis is performed using different E_T binning. The difference in these fits should be consistent with the statistical uncertainty on the fit using the default binning. Tables 7 and 8 and Figs. 18 and 19 show the result of fitting the purity using the different E_T bins, as well as the three different fitting functions. The fit results are all consistent with the previously quoted statistical and systematic uncertainties.

6 Cross Sections and Comparison to Theory

Combining the selections, efficiencies, and photon purities discussed in the previous sections, we evaluate the cross section using equation 1. For events with more that one photon candidate, only the two most energetic ones are used, applying the selection criteria to each separately. Table 9 shows the

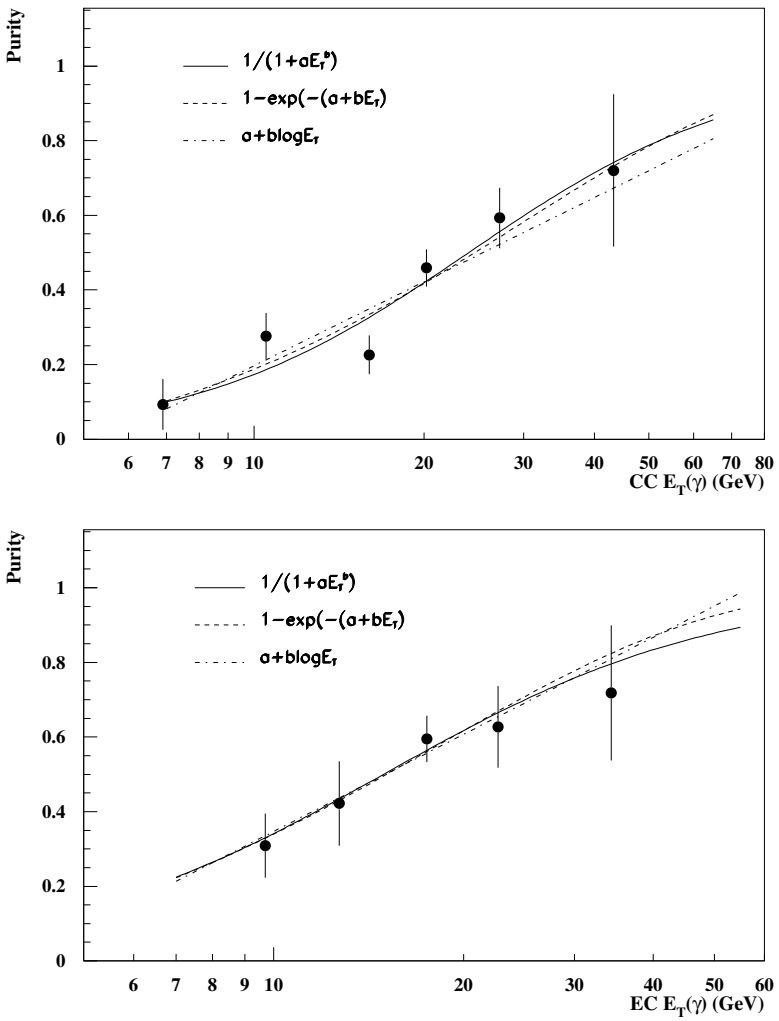

Figure 16: Purity using different fitting functions (a) CC and (b) EC.

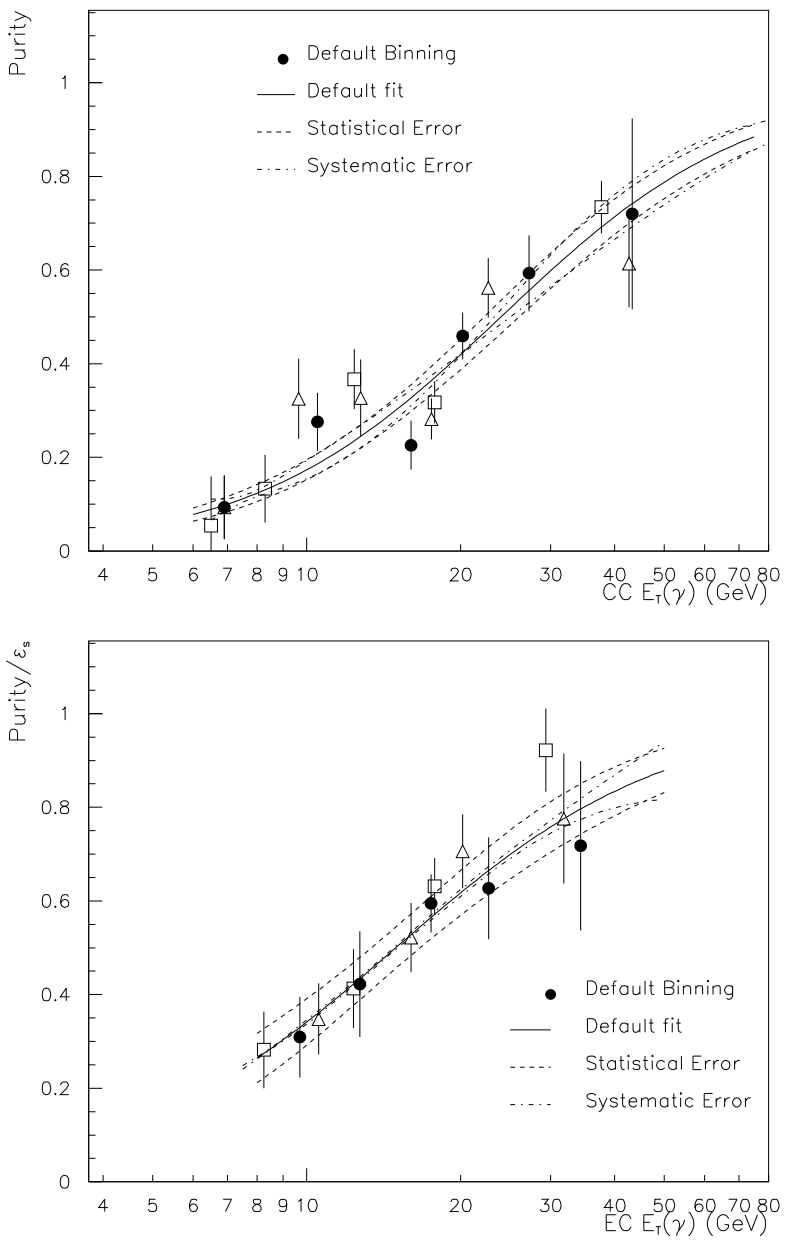

Figure 17: Statistical error from the default fit and band in systematic uncertainty from four possible fitting functions and three different bin selections for CC and EC data.

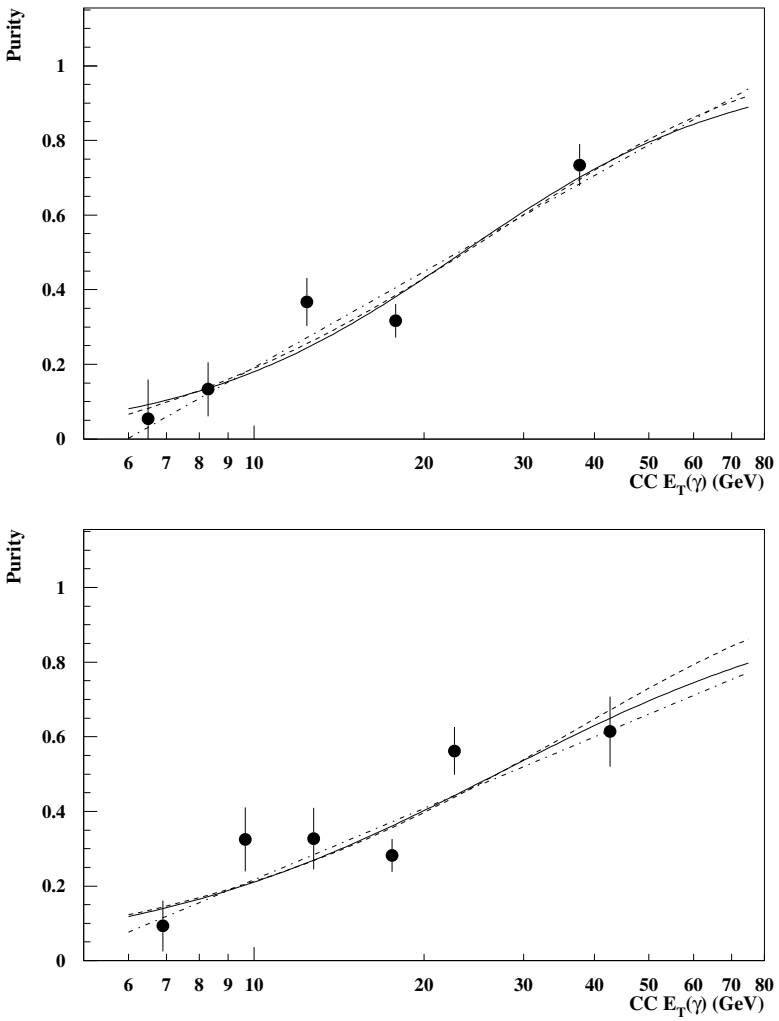

Figure 18: Purity with alternative E_T bins and three different fitting functions in the central rapidity region. The legend is the same as in Fig. 16.

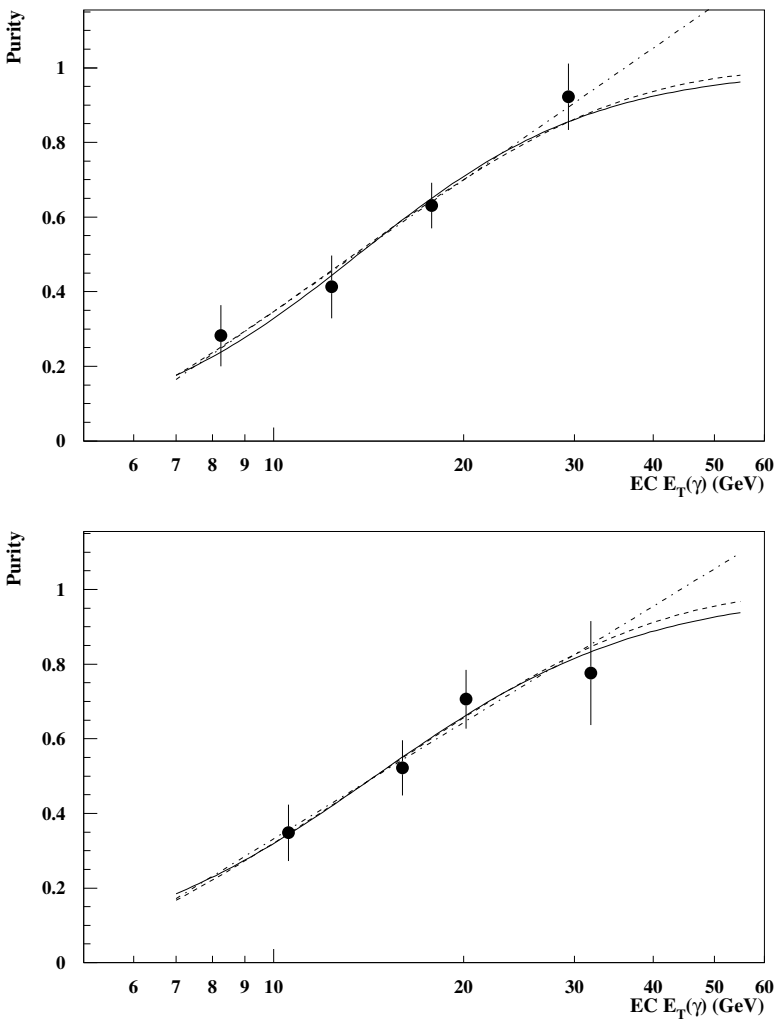

Figure 19: Purity with alternative E_T bins and three different fitting functions in the forward rapidity region. The legend to is the same as in Fig. 16.

number of candidates surviving each step for the CC and EC combined. The last cut, indicated as Filter, assures that there is a one to one correspondence between the energy of the photon candidate and the trigger energy range. For example, an event that fires only the low energy trigger but whose photon candidate is above the threshold for the medium energy trigger acceptance is not used to determine the cross section.

	$\|\eta\| < 0.9$		$1.6 < \|\eta\| < 2.5$	
Cut	Number of candidates	Lost events %	Number of candidates	Lost events %
Initial	64809	–	37960	–
$E_T > 6.0$ GeV	28239	56.4	20583	45.8
Vertex	23803	15.7	17304	15.9
$\eta^{det} + \phi$ crack	18378	22.8	16286	5.9
Track Veto	11486	37.0	6566	59.6
EM Fraction	9521	17.1	6293	4.2
χ^2	6553	31.2	4074	35.3
Isolation	5807	11.4	3884	4.7
Filter	3926	32.4	2294	40.9
Final Sample	**3926**	**93.9**	**2294**	**94.0**

Table 9: Number of photon candidates after each selection step.

Figure 20 displays the cross section for both rapidity regions, together with the theoretical prediction from Owens, Baer and Ohnemus [12] using the CTEQ4M parton distribution functions smeared with DØ photon energy resolutions. The results are tabulated in Tables 10 and 12. Tables 11 and 13 show the sources of the systematic uncertainty. Fig. 21 compares the data to the theoretical prediction in terms of the quantity (Data-Theory)/Theory. The theoretical prediction of Vogelsang *et. al.* using CTEQ5M and setting renormalization, factorization, and fragmentation scales equal to the highest transverse momentum parton in the event is also shown for comparison [13]. Fig. 22 compares the results of this analysis with results from UA2 [8].

E_T Range (GeV)	$\frac{<E_T>+E_T/2}{2}$	$\frac{d\sigma}{dE_T}(\frac{\text{pb}}{\text{GeV}})$	$\delta\sigma_{\text{stat}}(\%)$	$\delta\sigma_{\text{syst}}(\%)$
7-10	8.3	20100	4.5	69
10-13	11.3	3070	4.3	42
13-16	14.4	972	8.5	28
16-19	17.4	337	3.0	22
19-22	20.4	160	4.5	16
22-25	23.4	94.6	6.3	14
25-28	26.4	52.3	8.8	13
28-31	29.5	30.4	12	12
31-34	32.4	19.1	16	12
34-37	35.5	12.6	20	11
37-40	38.5	11.1	22	11
40-46	42.8	2.78	32	11
46-80	60.1	.710	28	8

Table 10: Differential cross section in the CC ($|\eta| < 0.9$) with statistical and systematic uncertainties.

E_T Range	$\mathcal{P}$(st)	$\mathcal{P}$(sy)	Frg	Esc	Trg	ϵ_s	Act	Trk	Lum
7-10	14	6	67	8	5	4	1	2	5
10-13	11	11	38	5	3	1	1	2	5
13-16	9	8	25	3	0	1	1	2	5
16-19	8	3	18	3	7	1	1	2	5
19-22	8	1	13	2	1	1	1	2	5
22-25	7	3	10	2	0	0	1	2	5
25-28	7	4	8	2	0	0	1	2	5
28-31	6	5	7	2	0	0	1	2	5
31-34	6	6	6	2	0	0	1	2	5
34-37	6	7	5	2	0	0	1	2	5
37-40	5	7	4	1	0	0	1	2	5
40-46	5	7	4	1	0	0	1	2	5
46-80	4	5	2	1	0	0	1	2	5

Table 11: Systematic uncertainty (in percent) in the CC. Sources of uncertainty include $\mathcal{P}/\epsilon_s$ due to statistics, $\mathcal{P}/\epsilon_s$ due to systematics, fragmentation, energy scale, trigger efficiency, acceptance, tracking efficiency, and luminosity.

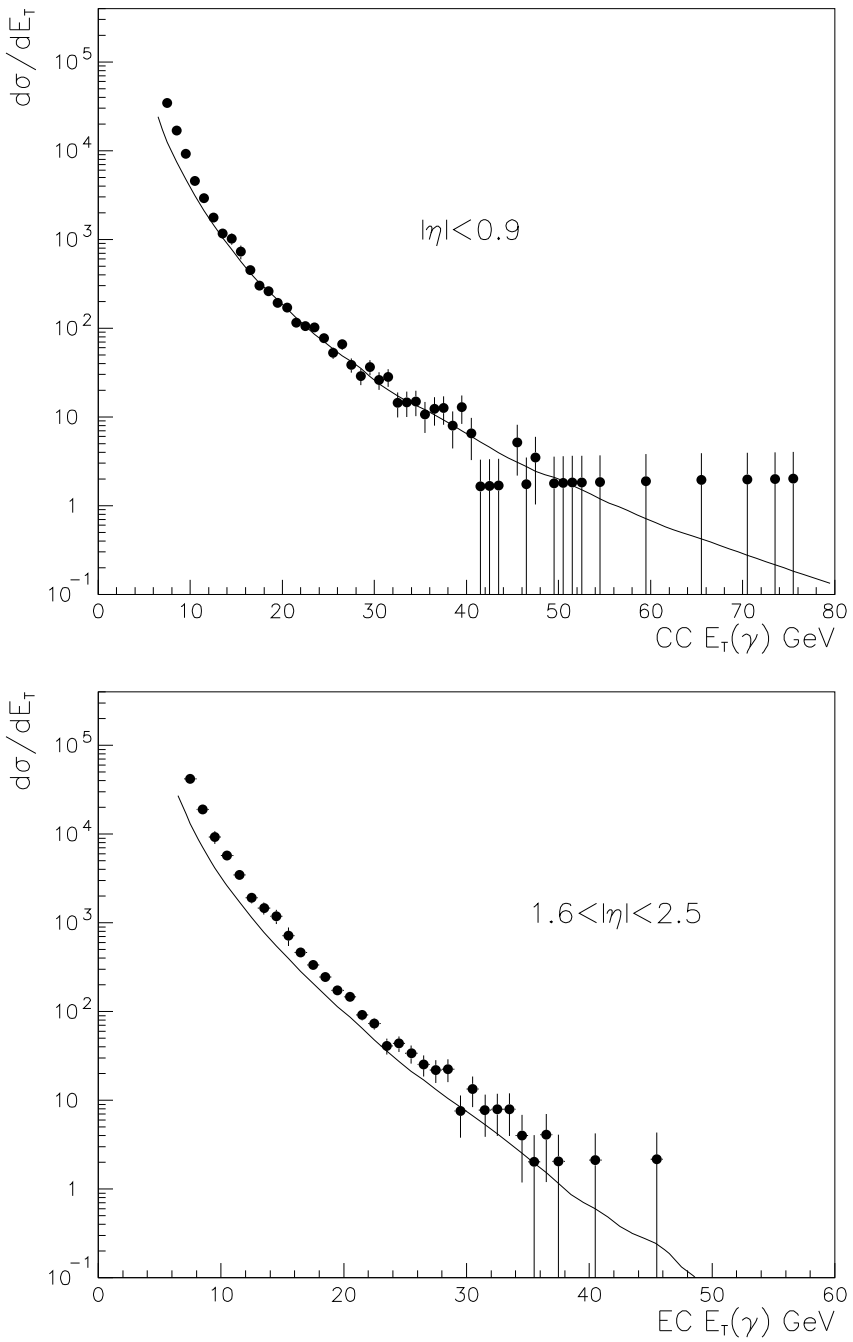

Figure 20: The isolated photon cross section, $d\sigma/dE_T d\eta$ vs. photon E_T for the central and forward rapidity regions. The errors are statistical and the curve is the theoretical prediction of CTEQ4M.

E_T Range (GeV)	$\frac{<E_T>+E_T/2}{2}$	$\frac{d\sigma}{dE_T}(\frac{\text{pb}}{\text{GeV}})$	$\delta\sigma_{\text{stat}}(\%)$	$\delta\sigma_{\text{syst}}(\%)$
7-10	8.3	23400	5.7	36
10-13	11.3	3700	7.7	25
13-16	14.4	1120	11	20
16-19	17.4	349	3.8	19
19-22	20.4	137	6.2	17
22-25	23.4	52.8	10	17
25-28	26.4	27.1	15	17
28-31	29.4	14.5	21	16
31-34	32.5	7.87	29	16
34-37	35.5	3.38	45	16
37-50	42.3	0.488	58	16

Table 12: Differential cross section in the EC ($1.6 < |\eta| < 2.5$) with statistical and systematic uncertainties.

E_T Range	$\mathcal{P}$(st)	$\mathcal{P}$(sy)	Frg	Esc	Trg	ϵ_s	Act	Trk	Lum
7-10	19	0	26	4	5	2	1	13	5
10-13	12	1	16	3	0	1	1	13	5
13-16	9	1	11	2	0	1	1	13	5
16-19	8	1	8	2	5	1	1	13	5
19-22	8	1	6	2	0	0	1	13	5
22-25	8	1	5	1	0	0	1	13	5
25-28	7	1	4	1	0	0	1	13	5
28-31	7	2	3	1	0	1	1	13	5
31-34	7	2	3	1	0	1	1	13	5
34-37	7	3	2	1	0	1	1	13	5
37-50	6	5	2	1	0	1	1	13	5

Table 13: Systematic uncertainty (in percent) in the EC. Sources of uncertainty include $\mathcal{P}/\epsilon_s$ due to statistics, $\mathcal{P}/\epsilon_s$ due to systematics, fragmentation, energy scale, trigger efficiency, acceptance, tracking efficiency, and luminosity.

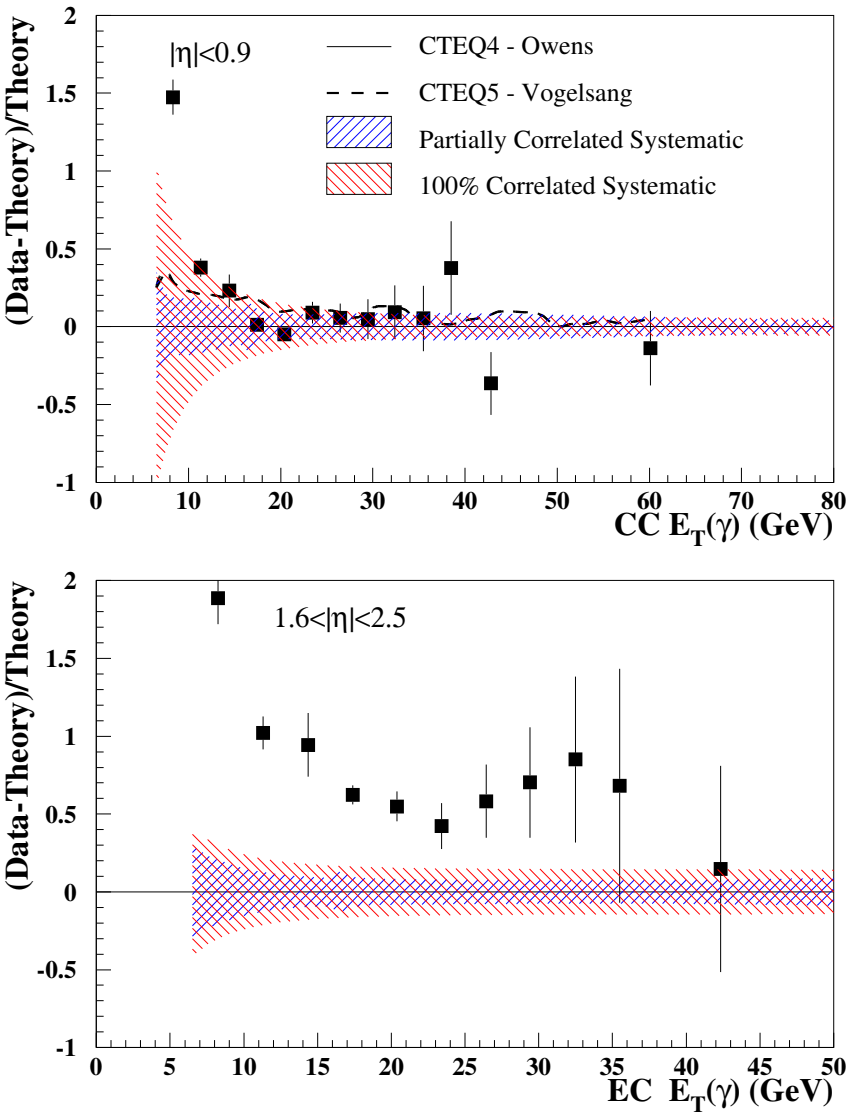

Figure 21: (Data-Theory)/Theory for the central (top) and forward (bottom) rapidity regions. The patterned regions show the partially correlated systematic uncertainty and the 100% correlated systematic uncertainty.

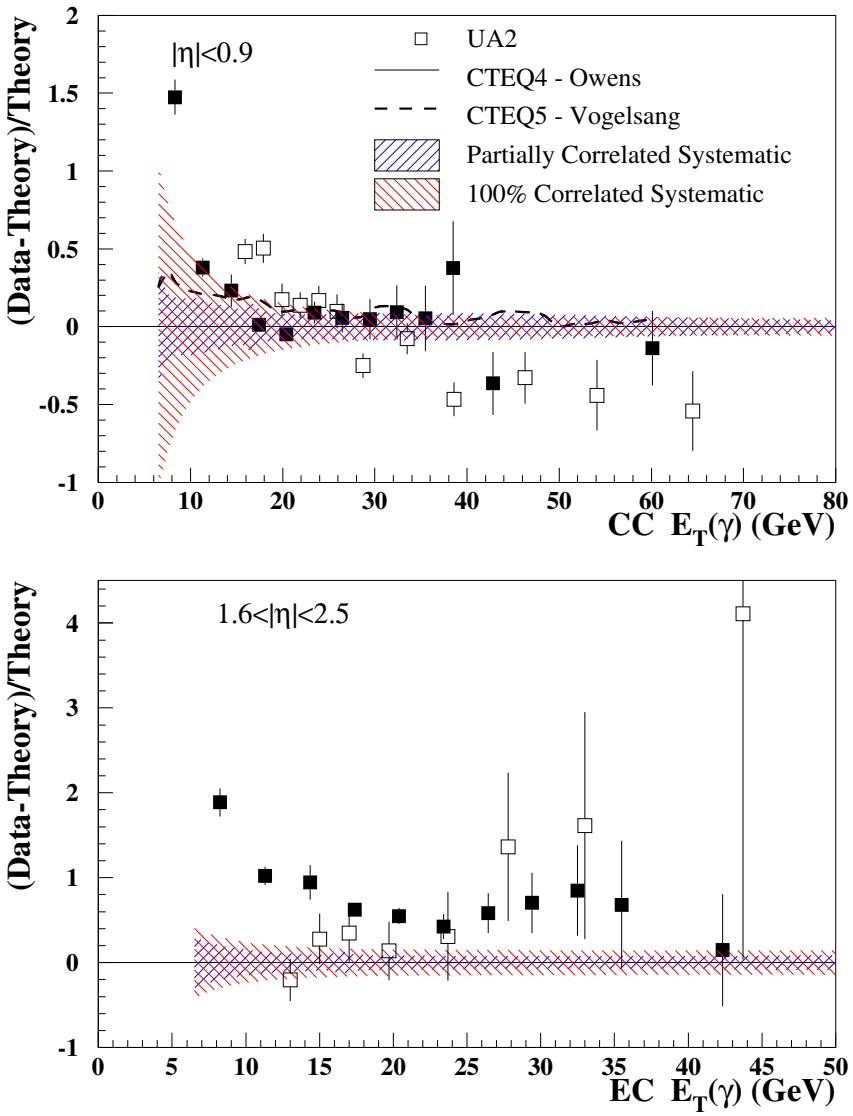

Figure 22: (Data-Theory)/Theory for the central (top) and forward (bottom) rapidity regions comparing to results from UA2. The errors on the UA2 data are statistical only.

7 Run 1A/1B Analysis Method

We also perform this analysis with modifications which make it more convenient to compare with the published 1800 GeV cross section. The primary difference between the method described in this note and the 1800 GeV measurement is that this analysis fits curves to purity and selection efficiency because of the fewer number of data events available to determine purity in different E_T regions (Section 5.2), while the 1800 GeV analysis used a bin-by-bin analysis. The larger data set at 1800 GeV ensures smaller statistical fluctuations. Here we describe the result of measuring the cross section at 630 GeV without fitting $\mathcal{P}/\epsilon_s$. In order to further facilitate comparison with the 1800 GeV analysis, we have used x regions that correspond to those used in the published 1800 GeV measurement, $.012 < x < .014$ (7.35 GeV $< E_T <$ 9.10 GeV), $.014 < x < .020$ (9.10 GeV $< E_T <$ 12.6 GeV), $.020 < x < .023$ (12.6 GeV $< E_T <$ 14.7 GeV), $.023 < x < .030$ (14.7 GeV $< E_T <$ 18.9 GeV), $.030 < x < .042$ (18.9 GeV $< E_T <$ 26.3 GeV), and $.042 < x$ (26.3 GeV $< E_T$). The selection efficiencies using this binning are shown in Fig. 23

Figs. 24 and 25 present the Monte Carlo fractional fits to the data in these E_T regions using the variable $\log(1 + \log(1 + E_1))$ as the discriminant in the CC and EC, respectively. Table 14 and Fig. 26 tabulate the results of the fits.

E_TRange (GeV)	CC Fit	EC Fit
7.35-9.10	24.2 ± 10.1	30.8 ± 10.5
9.10-12.6	30.0 ± 6.9	39.0 ± 8.4
12.6-14.7	44.0 ± 13.9	45.7 ± 18.5
14.7-18.9	24.8 ± 4.6	53.1 ± 6.4
18.9-26.3	51.7 ± 5.4	71.0 ± 9.1
>26.3	59.9 ± 14.6	68.6 ± 20.0

Table 14: Photon purity in the same x regions as the 1800 GeV published data.

Fig. 27 shows the result of $\mathcal{P}/\epsilon_s$ for the 1A/1B analysis method using the E_T binning which correlates with the 1800 GeV x regions. The curves in Fig. 27 show $\mathcal{P}/\epsilon_s$ using the functional forms and fit parameter values for $\mathcal{P}$ and ϵ_s derived and fitted in Sections 3.4 and 5.1, respectively, These curves are shown to help the reader compare the analysis method described

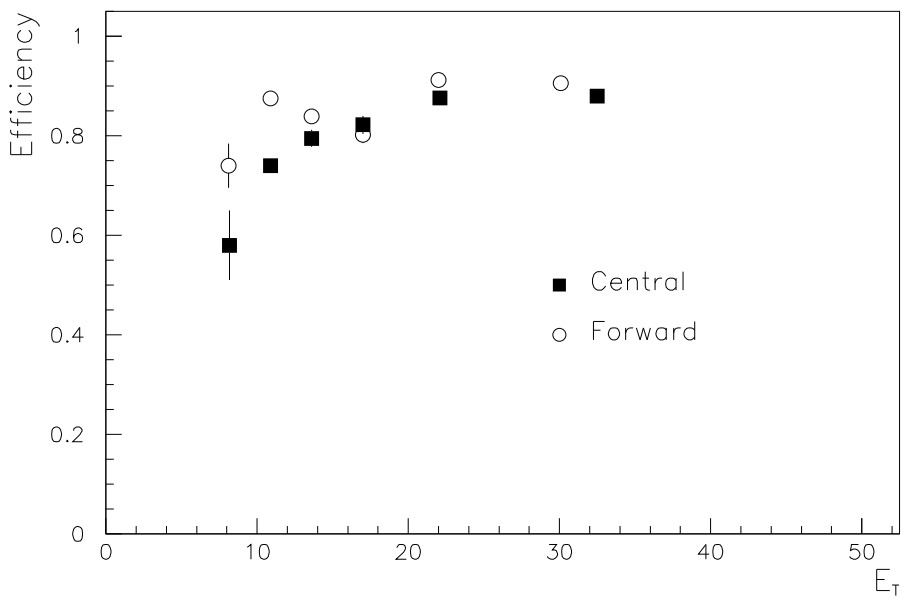

Figure 23: Photon selection efficiency for the central and forward regions in bins that correspond to the same x regions as the published 1A/1B data.

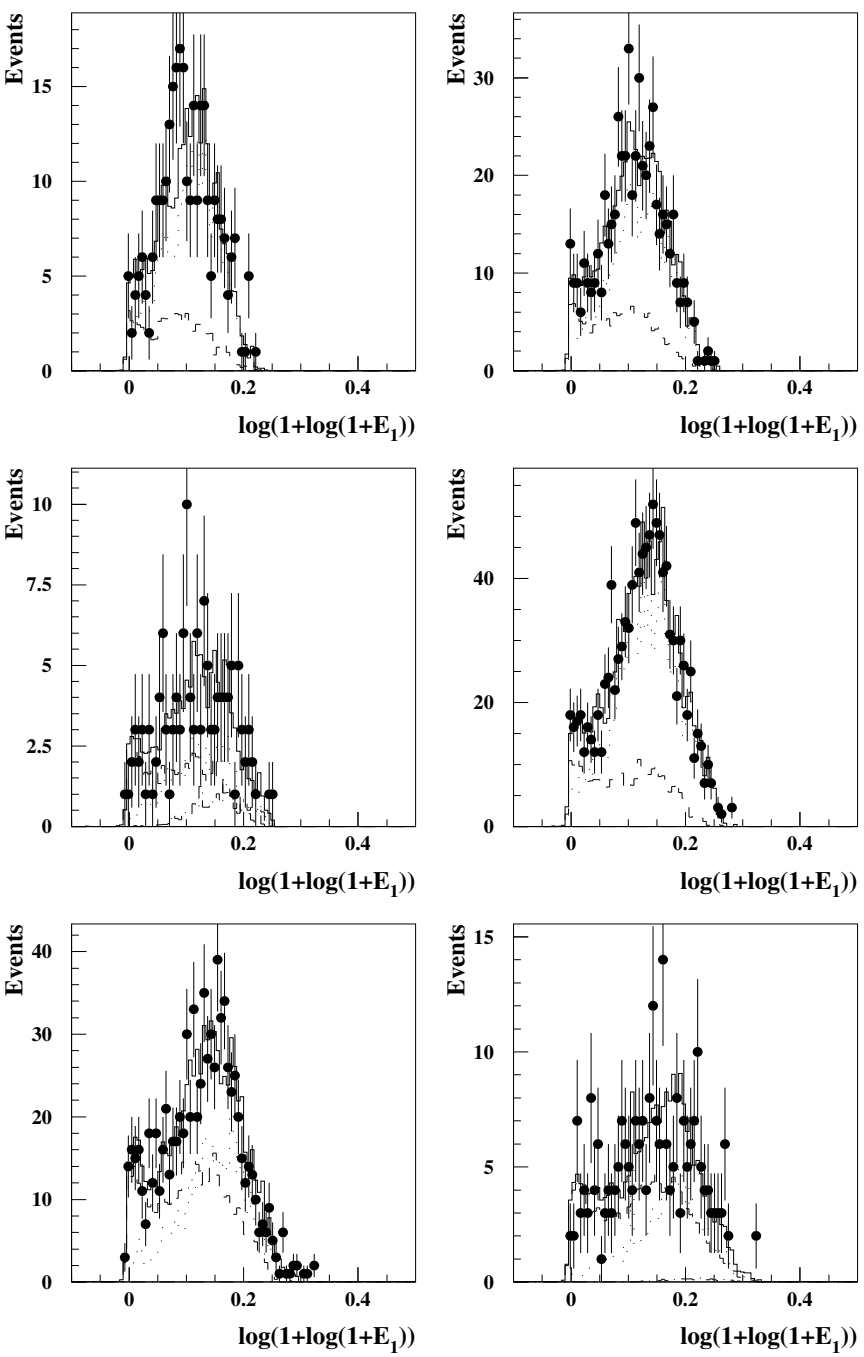

Figure 24: Distributions of $\log(1 + \log(1 + E_1))$ for the central η region in E_T bins of 7.35–9.10, 9.10–12.6, 12.6–14.7, 14.7–18.9, 18.9–26.3, and >26.3 GeV. The solid line is total MC fit to the data. The dashed line is the photon contribution, the dotted line is the jet background contribution, and the dash-dot line is the additional contribution from jets containing charged tracks.

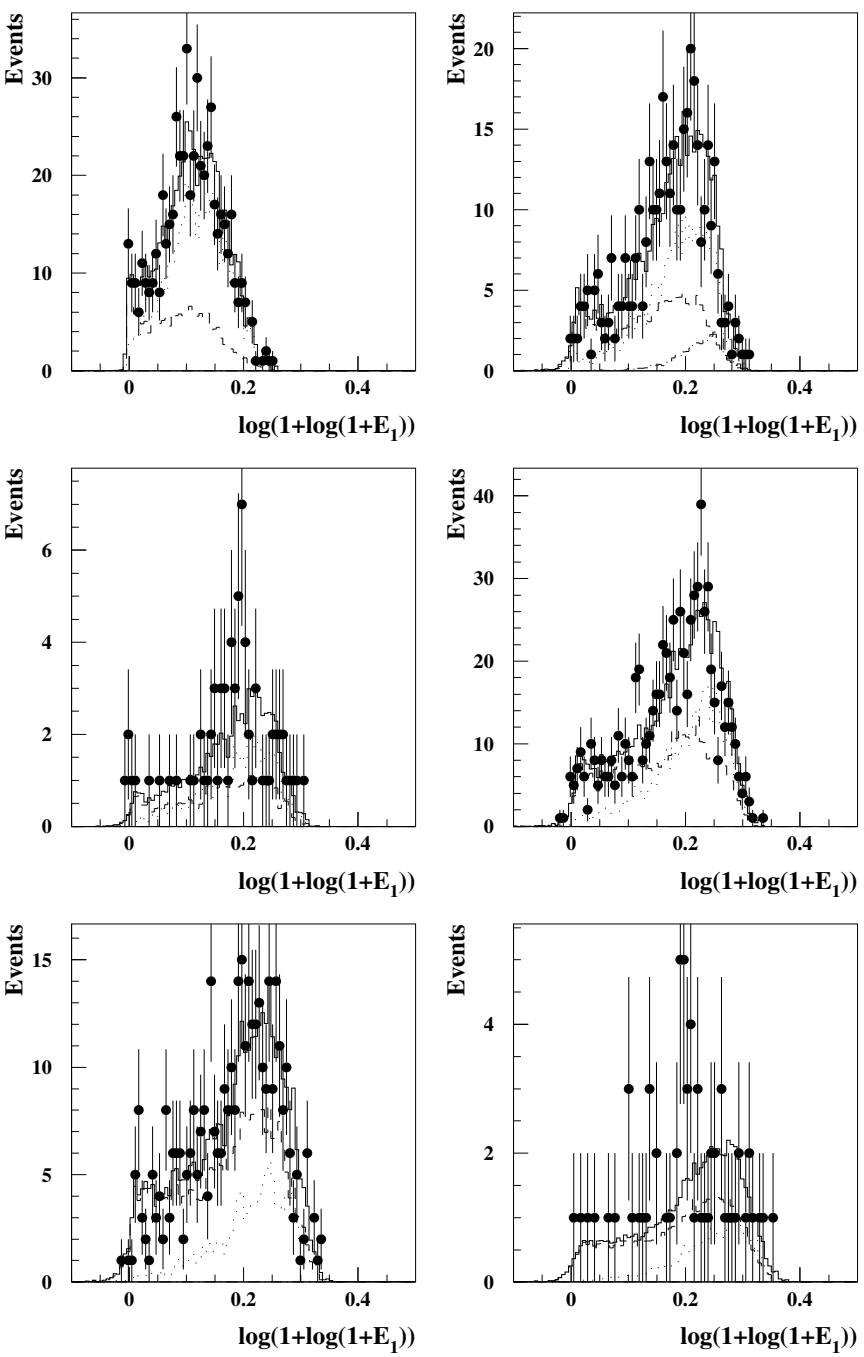

Figure 25: Distributions of $\log(1 + \log(1 + E_1))$ for the forward η region in E_T bins of 7.35–9.10, 9.10–12.6, 12.6–14.7, 14.7–18.9, 18.9–26.3, and >26.3 GeV. The solid line is total MC fit to the data. The dashed line is the photon contribution, the dotted line is the jet background contribution, and the dash-dot line is the additional contribution from jets containing charged tracks.

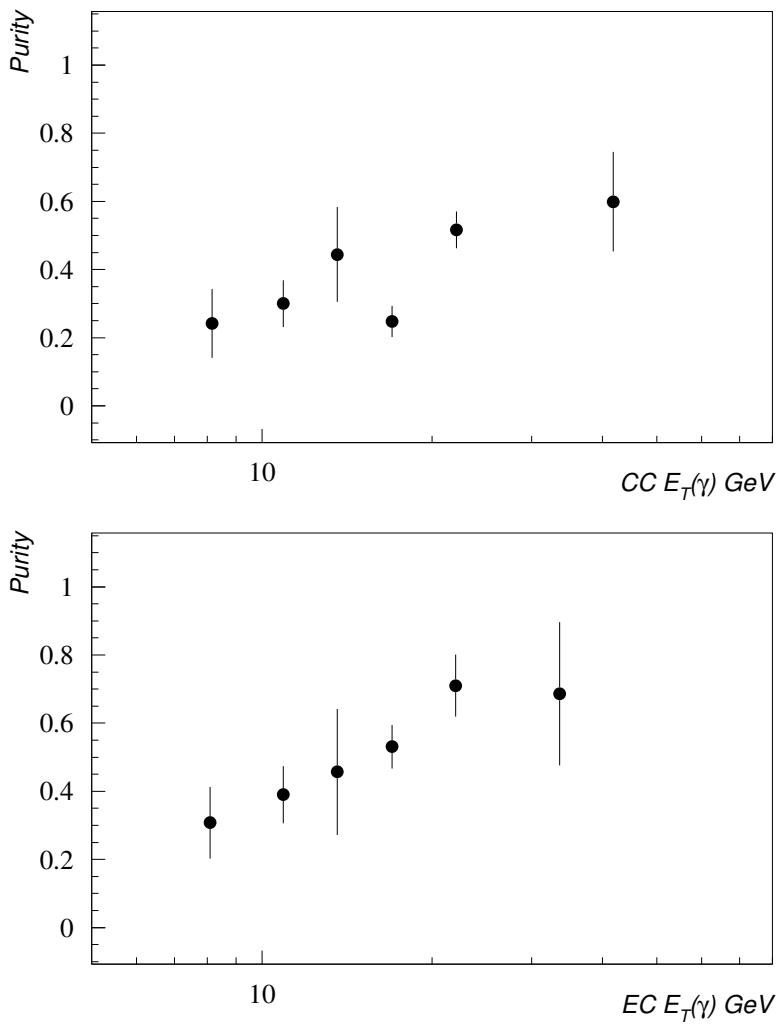

Figure 26: Photon purity for the central and forward regions using x regions that correlate with the published Run 1A/1B 1800 GeV data.

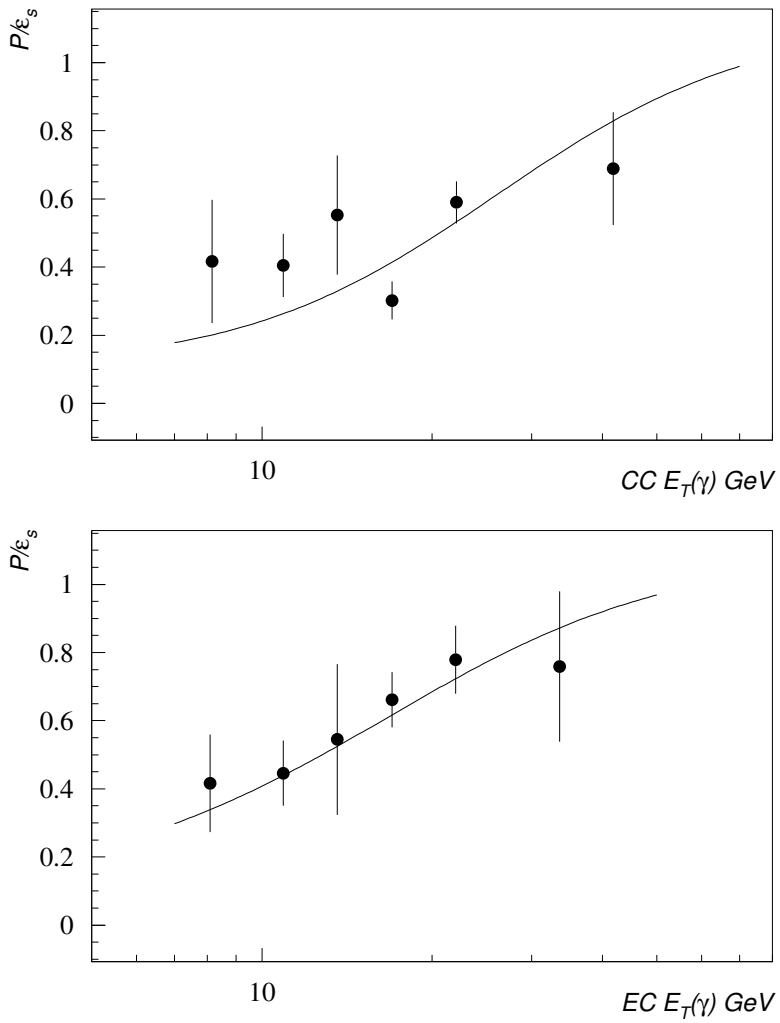

Figure 27: Photon purity divided by selection efficiency for the central and forward regions using x regions that correlate with the published Run 1A/1B 1800 GeV data. The curves are the fitted $\mathcal{P}/\epsilon_s$ results using the functions and fitted parameter values from Sections 3.4 and 5.1.

previously in this note (shown by the curves in this figure) and the 1A/1B analysis method (shown by the points in this figure) since the major difference in the two methods is whether or not the selection efficiency and the purity are fitted or simply used bin by bin.

For the published 1A/1B analysis, the uncertainty was quoted as a correlated and an uncorrelated uncertainty rather than as a statistical and a systematic uncertainty. Most of the uncorrelated uncertainty in this analysis comes from the purity divided by the selection efficiency as shown in Fig. 27.

The cross section derived using the 1A/1B analysis method is shown in Fig. 28. The low energy cross section in the central rapidity region is much higher using the 1A/1B 1800 GeV analysis method than that extracted from the default 630 GeV analysis method (see Section 6). In the lowest E_T bin (7.35-9.10 GeV) this is due to the low (and very uncertain) value of ϵ_s derived from the Monte Carlo below 8 GeV. For the next E_T bin (9.10-12.6 GeV) the main reason for the large value is that the $\mathcal{P}/\epsilon_s$ value fitted from the data fluctuates statistically to a higher value around 10 GeV. This local fluctuation is smoothed and minimized in the default analysis method because a smooth function of E_T is fit to the $\mathcal{P}/\epsilon_s$ points. Without this fitting, the high statistical fluctuation of the $\mathcal{P}/\epsilon_s$ point around 10 GeV causes a significant increase in the measured cross section. The results are tabulated in Tables 15 and 17.

E_T Range (GeV)	$\frac{<E_T>+E_T/2}{2}$	$\frac{d\sigma}{dE_T}(\frac{\text{pb}}{\text{GeV}})$	$\delta\sigma_{\text{uncor}}(\%)$	$\delta\sigma_{\text{cor}}(\%)$
7.35- 9.1	8.2	42600	44	43
9.1-12.6	10.9	7410	23	31
12.6-14.7	13.6	2130	31	24
14.7-18.9	17.0	360	21	19
18.9-26.3	22.1	133	10	14
26.3-76.0	41.8	6.35	24	8

Table 15: Differential cross section in the CC with uncorrelated and correlated errors.

Fig. 29 shows the difference between the experimental and theoretical differential cross sections using the theory of Owens *et. al.* The correlated uncertainty includes contributions from the uncertainty on the geometric acceptance, the luminosity, the tracking efficiency, and the fragmentation model. The uncorrelated uncertainty includes the uncertainties due to statistics, purity fitting, the efficiency of the selection criteria, and the trigger efficiency.

	Uncorrelated			*Correlated*				
E_T **Range**	$\mathcal{P}$	ϵ_s	**Trg**	**Frg**	**Esc**	**Act**	**Trk**	**Lum**
7.35- 9.1	42	12	6	42	6	1	2	5
9.1-12.6	23	2	4	30	4	1	2	5
12.6-14.7	31	2	0	23	3	1	2	5
14.7-18.9	19	2	9	18	3	1	2	5
18.9-26.3	10	1	0	13	2	1	2	5
26.3-76.0	24	1	0	6	2	1	2	5

Table 16: Sources of correlated and uncorrelated uncertainty in the CC (in percent).

E_T **Range (GeV)**	$\frac{<E_T>+E_T/2}{2}$	$\frac{d\sigma}{dE_T}(\frac{\text{pb}}{\text{GeV}})$	$\delta\sigma_{\text{uncor}}(\%)$	$\delta\sigma_{\text{cor}}(\%)$
7.35- 9.1	8.1	30200	35	28
9.1-12.6	10.9	5640	22	21
12.6-14.7	13.6	1310	41	18
14.7-18.9	17.0	579	14	16
18.9-26.3	22.0	93.0	13	15
26.3-47.0	33.6	4.82	31	14

Table 17: Differential cross section in the EC with uncorrelated and correlated errors.

	Uncorrelated			*Correlated*				
E_T **Range**	$\mathcal{P}$	ϵ_s	**Trg**	**Frg**	**Esc**	**Act**	**Trk**	**Lum**
7.35- 9.1	34	6	6	24	3	1	13	5
9.1-12.6	22	1	0	16	3	1	13	5
12.6-14.7	40	2	0	11	2	1	13	5
14.7-18.9	12	2	6	8	2	1	13	5
18.9-26.3	13	1	0	5	2	1	13	5
26.3-47.0	20	1	0	3	1	1	13	5

Table 18: Sources of correlated and uncorrelated uncertainty in the EC (in percent).

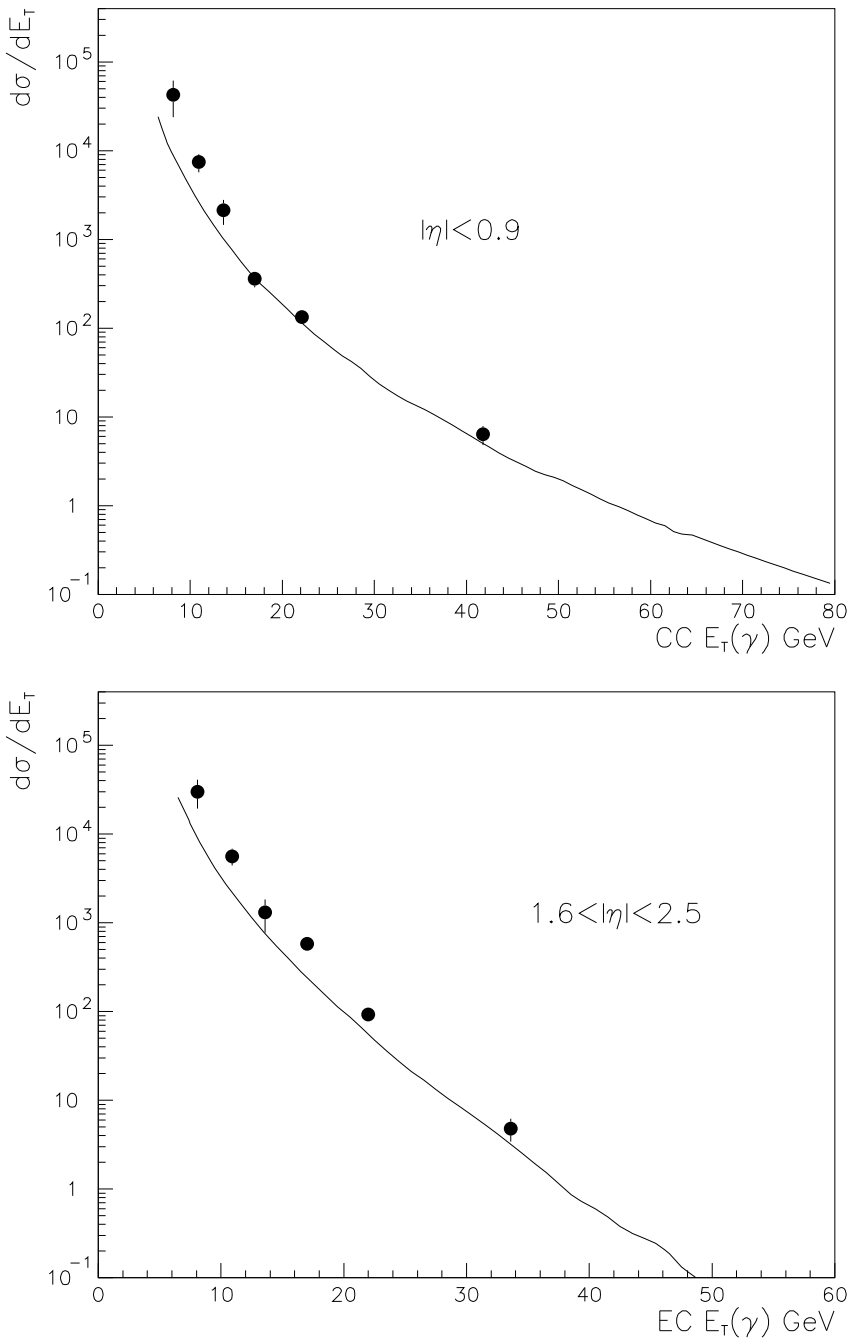

Figure 28: The isolated photon cross section, $d\sigma/dE_T\ d\eta$ vs. photon E_T for the central and forward rapidity regions using the 1A/1B analysis method. The errors are the total uncorrelated error and the curve is the theoretical prediction of CTEQ4M.

Contributions to the uncertainty from each of the sources is shown in Tables 16 and 18. The lowest energy bin is in a range of $7.35 < E_T < 9.10$ GeV/c. Because this is lower than the minimum energy for which a reasonable uncertainty can be calculated, (see Sections 3.1 and 3.4), Fig. 29 is replotted in Fig. 30 without the lowest energy bin. Finally, the same data is plotted with the UA2 data and CTEQ5 as implemented by Vogelsang in Fig. 31

8 Conclusions

We measure the inclusive cross section for isolated photons at $\sqrt{s} = 630$ GeV in the central ($|\eta| < 0.9$) and forward ($1.6 < |\eta| < 2.5$) rapidity regions. We compare the results to theoretical predictions by Owens using CTEQ4M and Vogelsang using CTEQ5.

Both theoretical descriptions show good agreement with the data in the central rapidity region for a limited region of E_T between about 15 and 40 GeV. However, neither theory reproduces the data at lower E_T where the production cross section is higher than the theory. In the forward region, the measured cross section is higher than the theory for most of the experimentally accessible region, particularly for $E_T < 20$ GeV. Both theoretical predictions fail to describe the shape of the data in both the central and forward rapidity regions, particularly for low values of E_T.

The agreement with UA2 data is better than the agreement with the theory. Except for the lowest E_T bins measured by UA2 the two experiments agree within uncertainties. In particular, the agreement in the CC is quite good. Both experiments demonstrate the same shape, with a higher cross section than theory at low E_T and a lower cross section than the theory at higher E_T.

A qualititive assessment of the agreement between data and theory is made by determining the χ^2 of the data with respect to the theory using the complete covariance matrix.

For each parameter in the cross section a fractional error matrix is determined taking all correlations into account. These error matrices are added together to produce a single fractional error matrix $\boldsymbol{A}$. The correlation terms of this fractional error matrix are shown in Fig. 32, where the uncorrelated statistical error has not been added and the different bins correspond to the energy bins shown in Tables 10– 13 and Figs. 20– 22. The total error matrix ($\boldsymbol{V}$) is given by

$$V_{i,j} = A_{ij} T_i T_j + B_{ij} D_i D_j$$

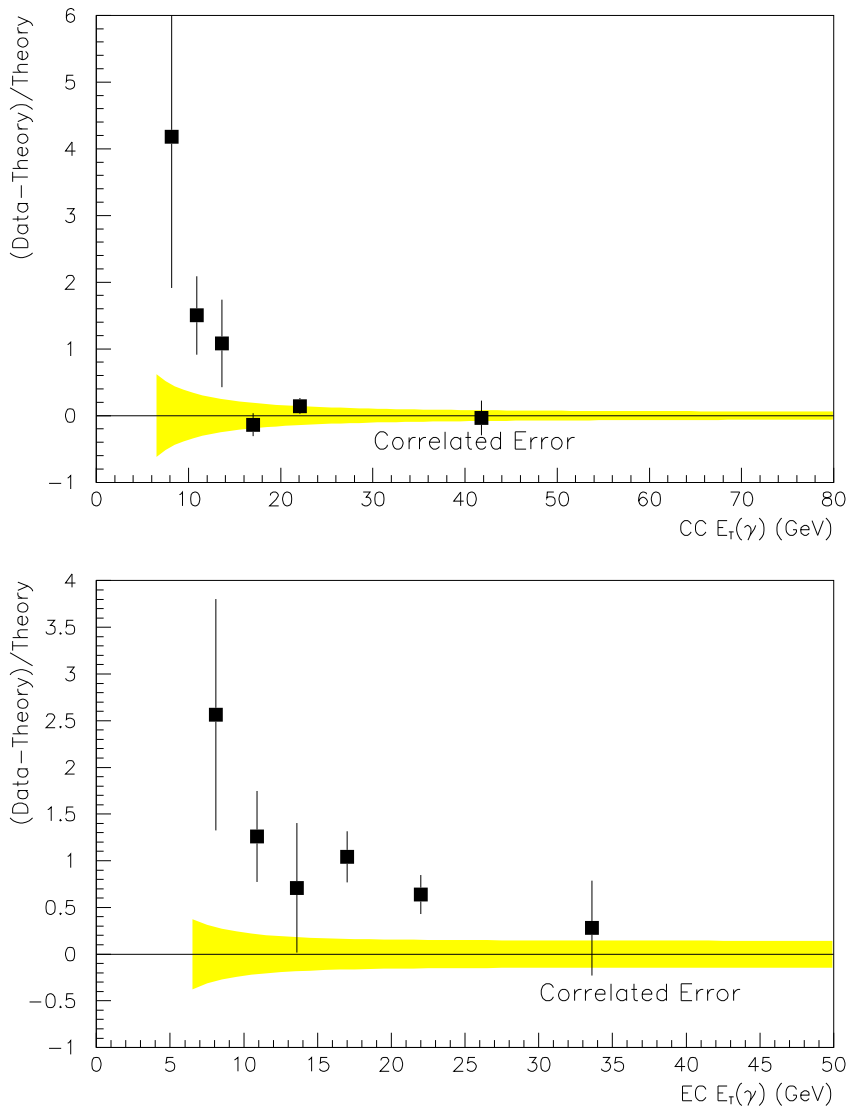

Figure 29: (Data-Theory)/Theory for the central (top) and forward (bottom) rapidity regions. The error bars indicate the uncorrelated uncertainty and the shaded region shows the correlated uncertainty.

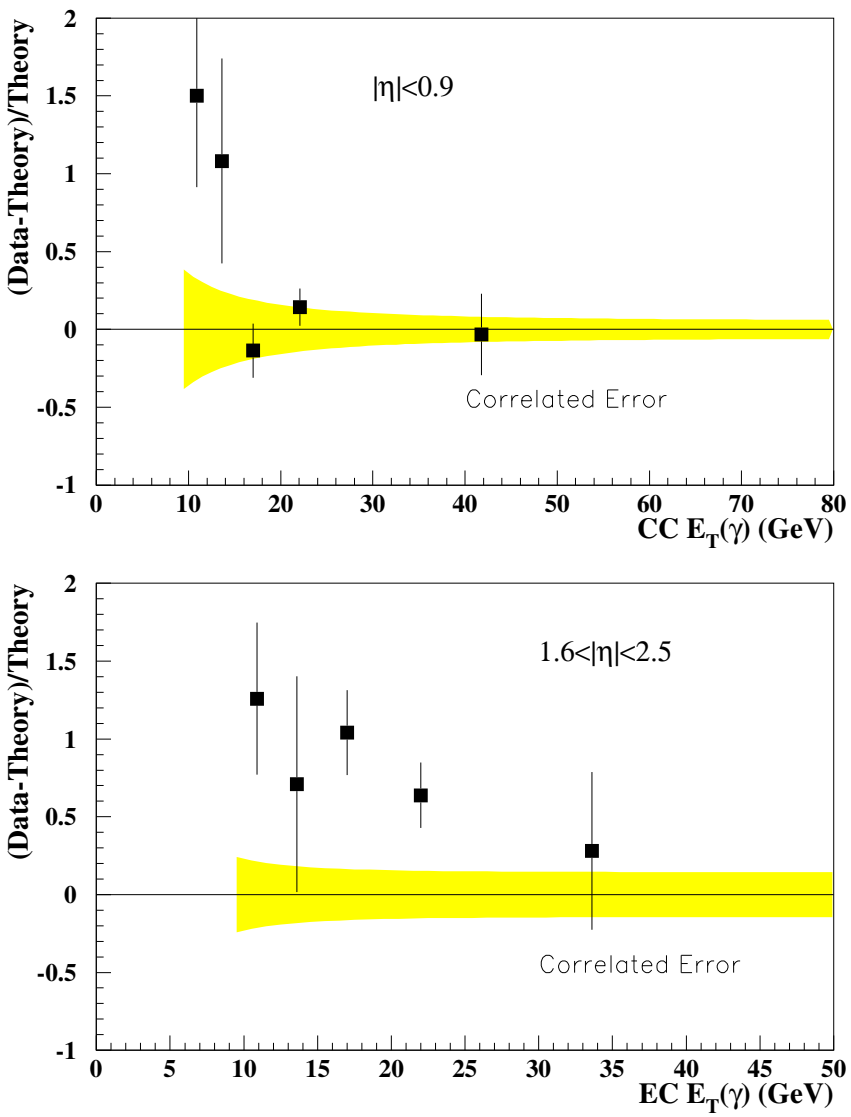

Figure 30: Same as Fig. 29 but without the lowest energy bin plotted.

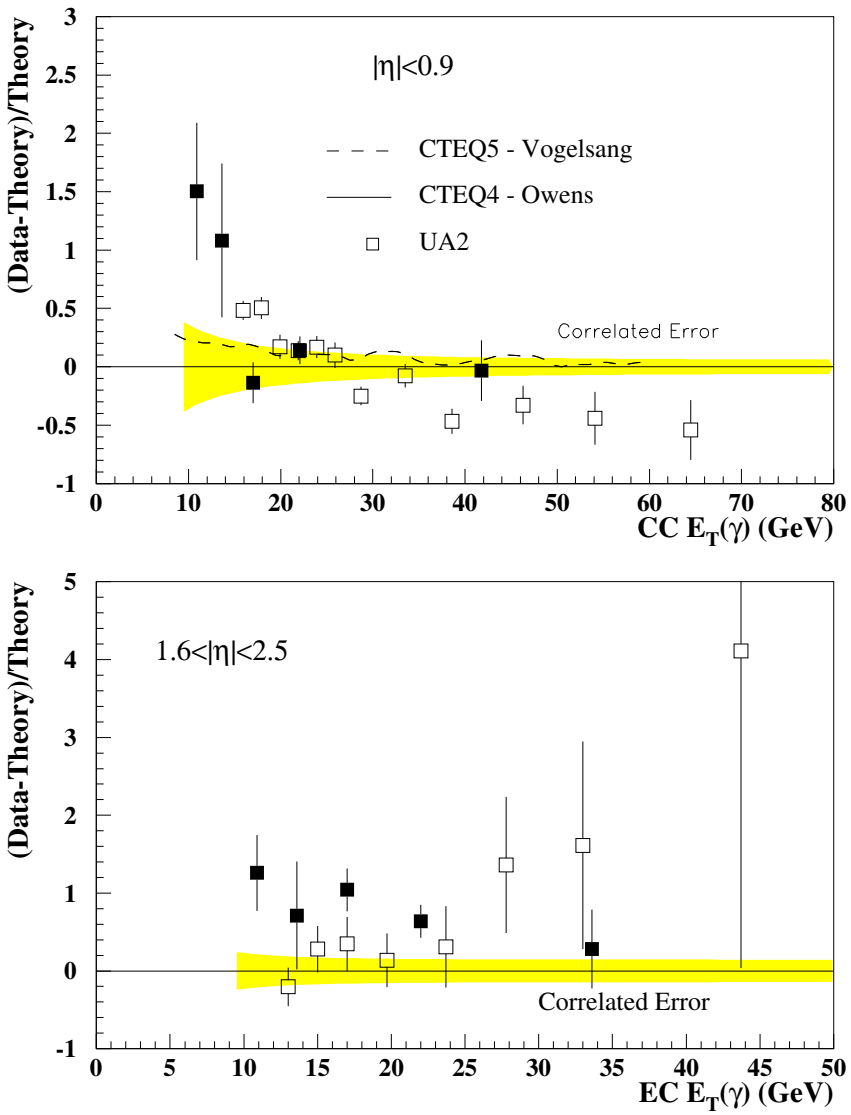

Figure 31: Same as Fig. 30 showing the UA2 data and CTEQ5 as implemented by Vogelsang.

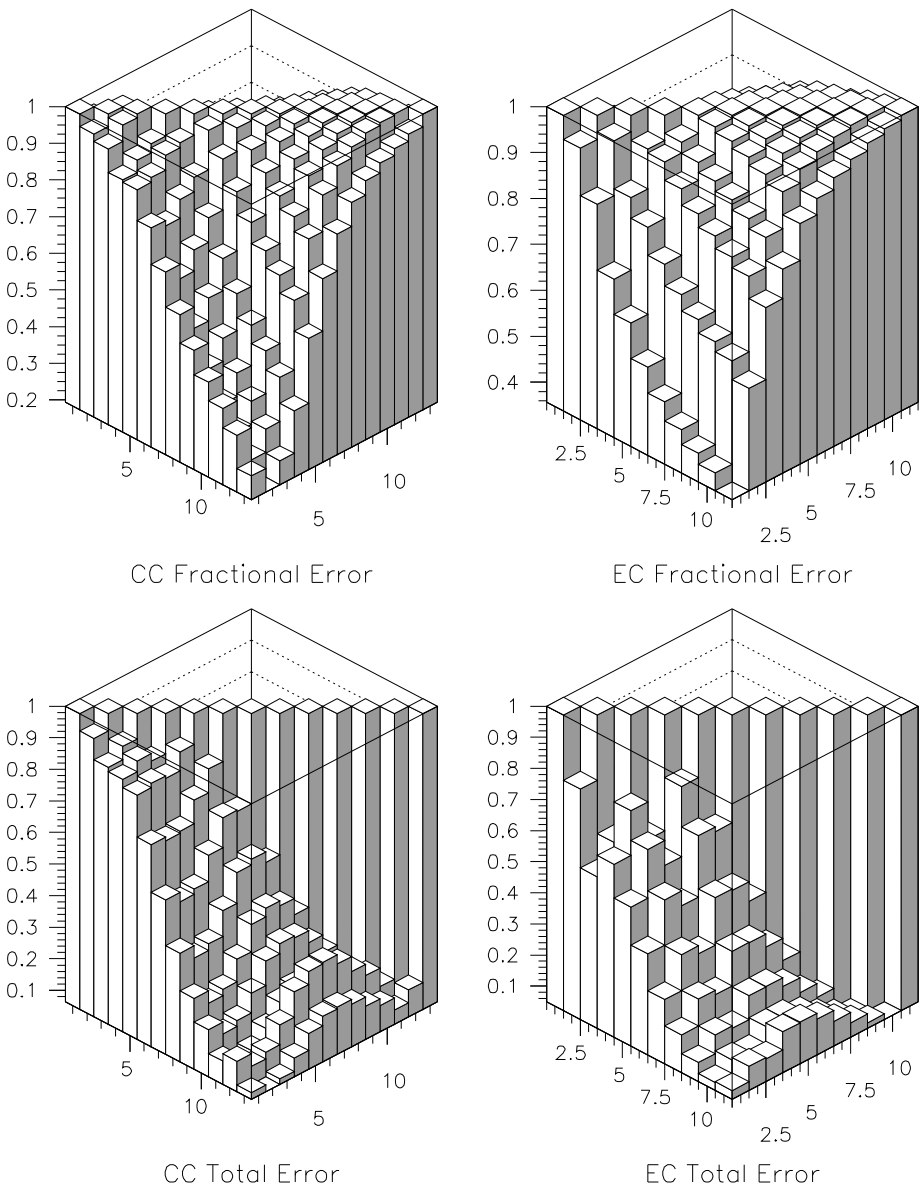

Figure 32: Correlation terms for error matrix. The top plots show the fractional systematic error matrix and the bottom plots show the total error matrix including the uncorrelated statistical errors.

where T_i and T_J are the theoretical cross sections in the ith and jth E_T bin, D_i and D_j are the measured cross section in the E_T bins, B_{ij} are the matrix elements of the fractional statistical error matrix (which is diagonal). The correlation terms for this total error matrix are also shown in Fig. 32. The χ^2 value is calculated using the equation

$$\boldsymbol{\chi^2 = (D - T)^T \, \overline{V}^{-1} (D - T).}$$

Using the data and theory in Fig. 21 we find a χ^2 value of 26.9 (25.8) for 13 (11) degrees of freedom in the CC (EC). Therefore, the probability that the theory fits the data is 1.2% (0.7%) in the CC (EC). Clearly the theory does not fit the data very well.

A similar statistical analysis has been done using the Run 1A/1B method. From the information shown in Figs. 29 and Figs. 30, we calculate a χ^2 value of 12.7 (18.5) for 6 (6) degrees of freedom in the CC (EC), or a χ^2 value of 9.77 (12.6) for 5 (5) degrees of freedom in the CC (EC), respectively. From this analysis, the probability that the theory fits the data is 4.8% (0.5%) or 8.2% (2.7%) in the CC (EC), respectively.

A Monte Carlo Statistics

It was mentioned in Section 2.2, that the MC statistics were increased by overlaying eight to ten different zero bias events onto the same GEANT event. We have recalculated the photon purities for the central regions, but allowing each PYTHIA event to be used only once in the analysis. The comparison of results with the enlarged MC sample is summarized in Table 19. The tests in this appendix were performed by fitting the purity distributions in the CC region using smoothed HBOOK Monte Carlo distributions and MINUIT [6].

E_TBin (GeV)	E_T(GeV)	Case A	Case B
8-13	10.6 ± 1.2	14.8 ± 5.70	20.2 ± 5.2
13-18	16.5 ± 1.1	9.4 ± 4.8	12.9 ± 4.5
18-23	19.9 ± 1.4	32.2 ± 4.9	27.8 ± 4.5
23-33	26.3 ± 2.6	37.5 ± 7.7	28.4 ± 7.1
>33	37.6 ± 3.8	69.8 ± 20.6	72.4 ± 25.8

Table 19: Purity results with (case A) and without (case B) several noise files overlayed for the same PYTHIA event.

B Center of Mass Energy

The selection efficiency and the purity for this analysis is somewhat dependent on the Monte Carlo simulation. We expect that the Monte Carlo generated at 1800 GeV should adequately describe the data for these variables. This appendix investigates, in more detail, how well the Monte Carlo generated at 1.8 TeV describes the data at 630 GeV.

B.1 Calorimeter Energy

The determination of the purity is very dependent on E_1, the energy deposited in the first electromagnetic section of the calorimeter. A comparison of the mean E_1 of Run 1B at 1800 GeV and Run 1C at 630 GeV before and after imposing selection requirements, is shown in Figs. 33 and 34. Except for high transverse energies in the EC before selections, there is good agreement between the two data sets. Since the correction is applied after cuts, and since most of the photons lie below 20 GeV, we expect that the Run 1B Monte Carlo adequately simulates the E_1 energy distributions in Run 1C.

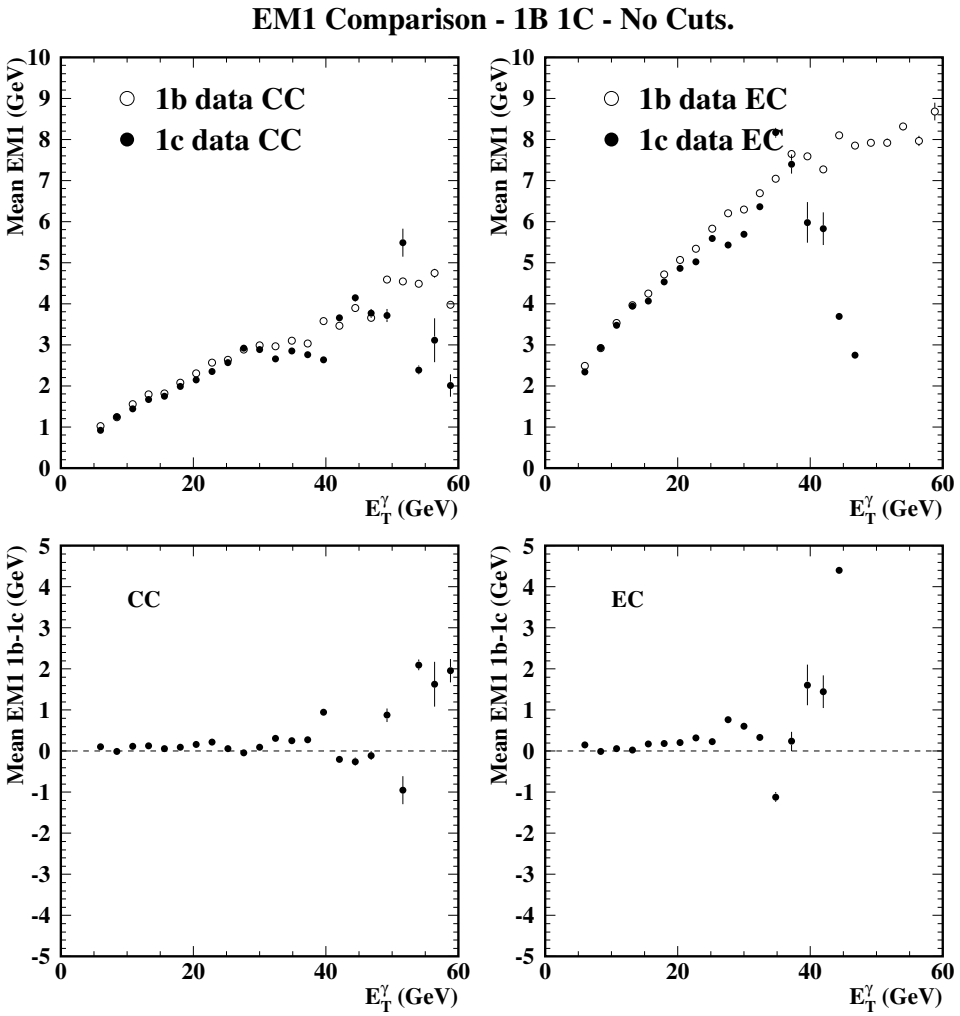

Figure 33: Comparison of E_1 energy for Run 1B at 1800 GeV and Run 1C at 630 GeV, before imposing photon selection criteria.

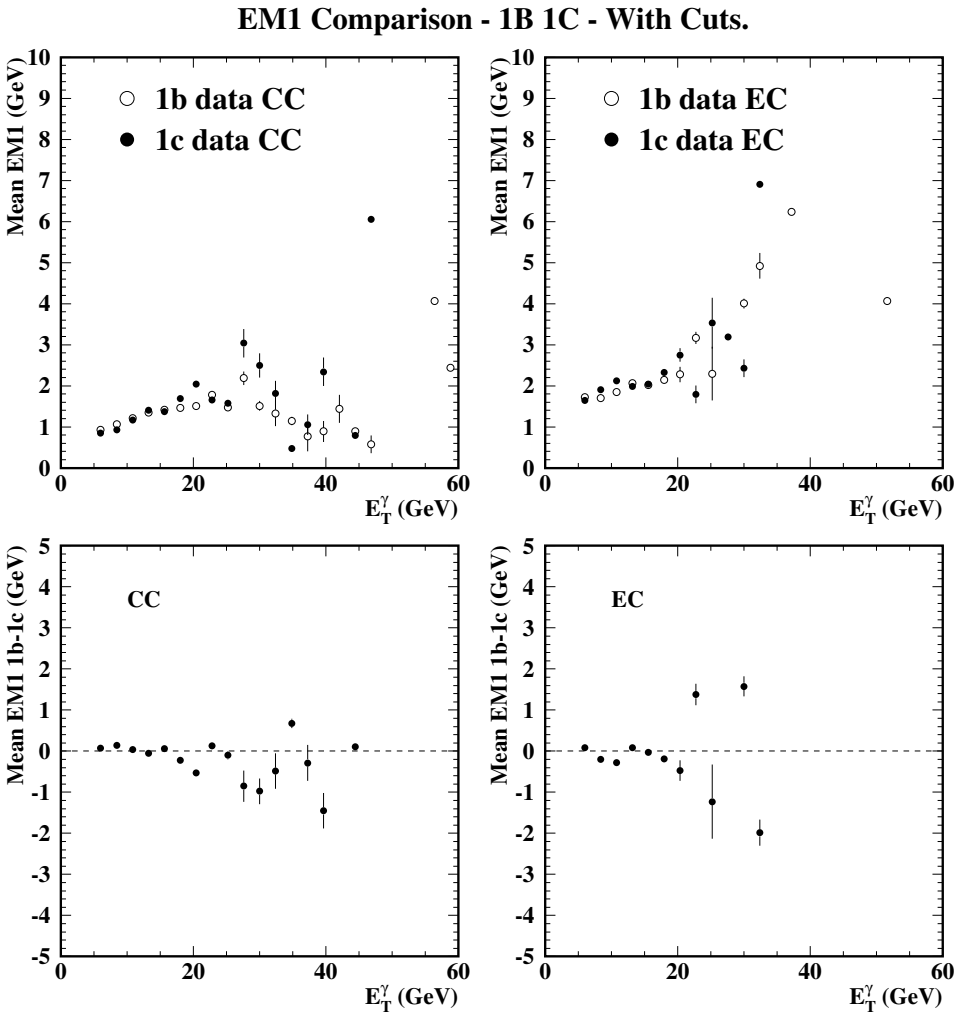

Figure 34: Comparison of E_1 energy for Run 1B at 1800 GeV and Run 1C at 630 GeV, after imposing photon selection criteria.

B.2 Selection Distributions

We also compare various Monte Carlo and data variables used for selecting events. The comparison is made in six E_T regions that do not cross any trigger boundaries or any MC generation boundaries (7–8–10–14–16–20–40 GeV). The lowest E_T region is not used in the cross section measurement and so agreement is less important than in the higher regions. For each variable we plot the data along with the Monte Carlo photons and jets scaled to have the same number of events as the data in each particular E_T region as shown in Figs. 35 through 40. A minimum requirement for the Monte Carlo to accurately describe the data is that the distribution of data points should fall somewhere between the photon and the jet distributions since the data is a mixture of the two. Two sets of photon Monte Carlo are compared with the data: the fully simulated events used for efficiency studies, and the events fully simulated only in a cone of $R = 0.7$ around each electromagenetic cluster used for the purity determination. It is expected that the latter should not adequately describe certain kinematic variables, such as missing E_T. The Monte Carlo jet data is fully simulated only in a cone of $R = 0.7$ around each electromagenetic cluster. The Monte Carlo photons and jets have considerabley more events than the data and, consequently, have statistical uncertainties much smaller than the data. The fully simulated events vary from one-sixth the number of data events in the lowest E_T bin to ten times the number of data events in the highest E_T bin.

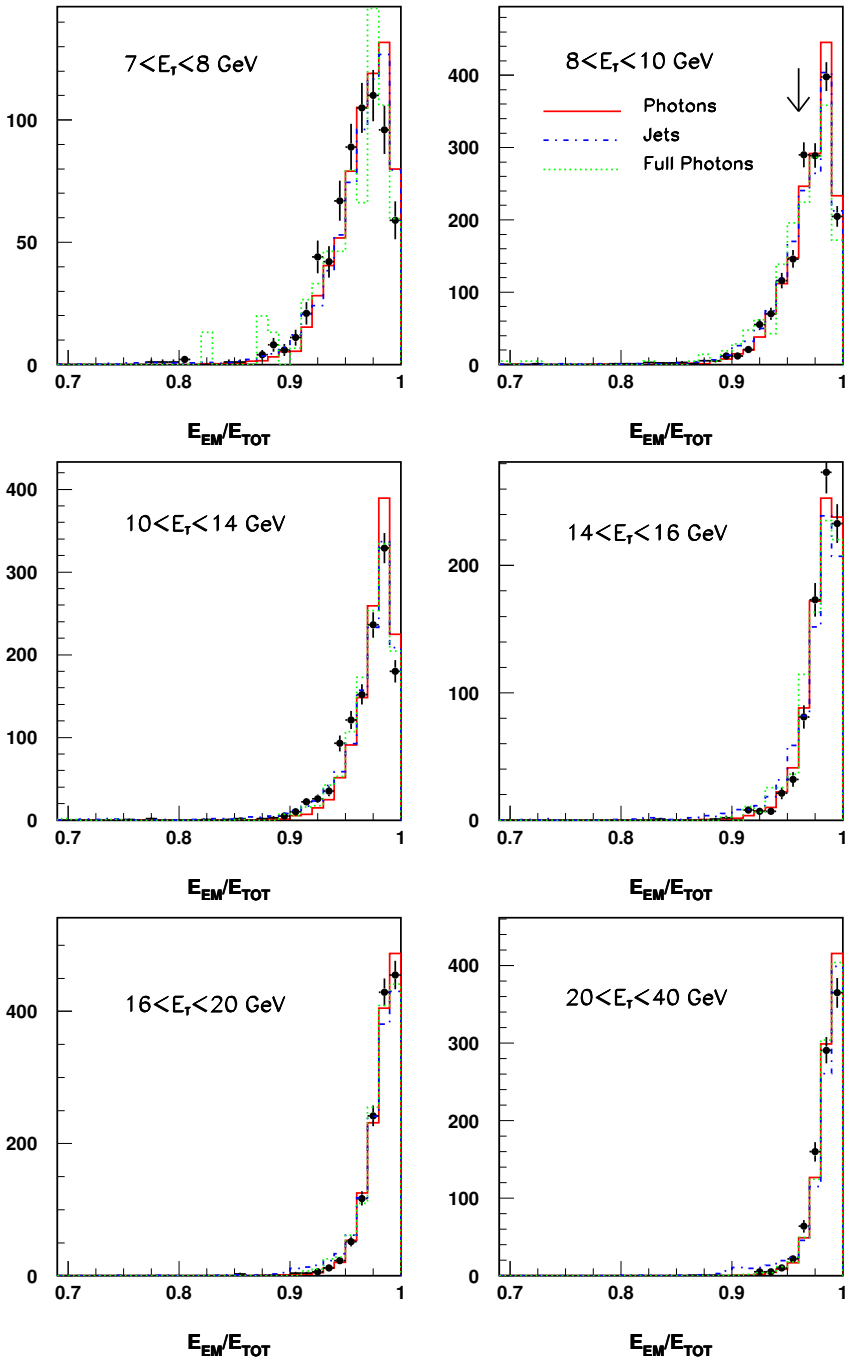

Figure 35: Comparison of Monte Carlo and data for the electromagnetic fraction in the CC. The key and selection criteria (indicated with an arrow) shown in one E_T region is identical for all E_T regions.

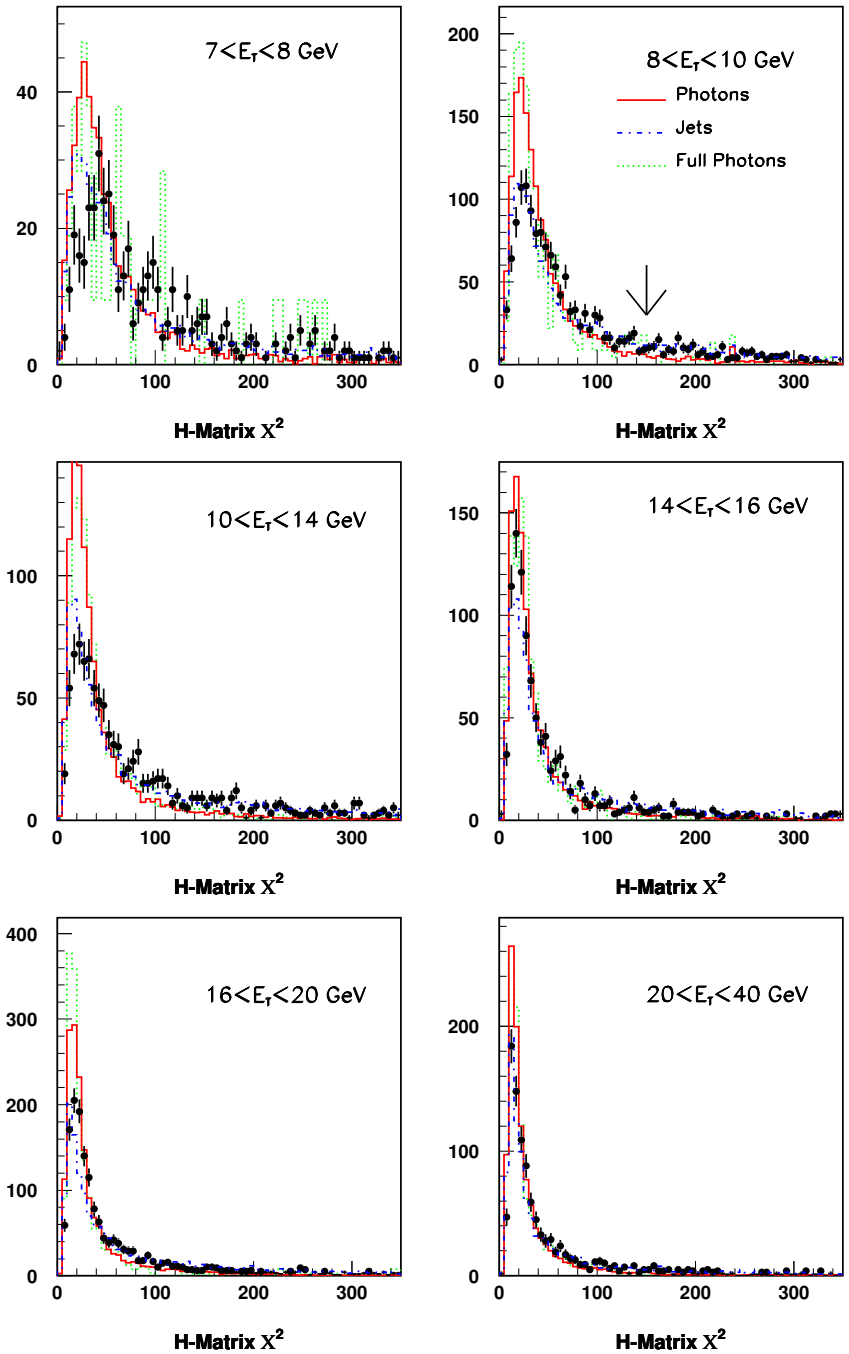

Figure 36: Comparison of Monte Carlo and data for the H-Matrix χ^2 in the CC. The key and selection criteria (indicated with an arrow) shown in one E_T region is identical for all E_T regions.

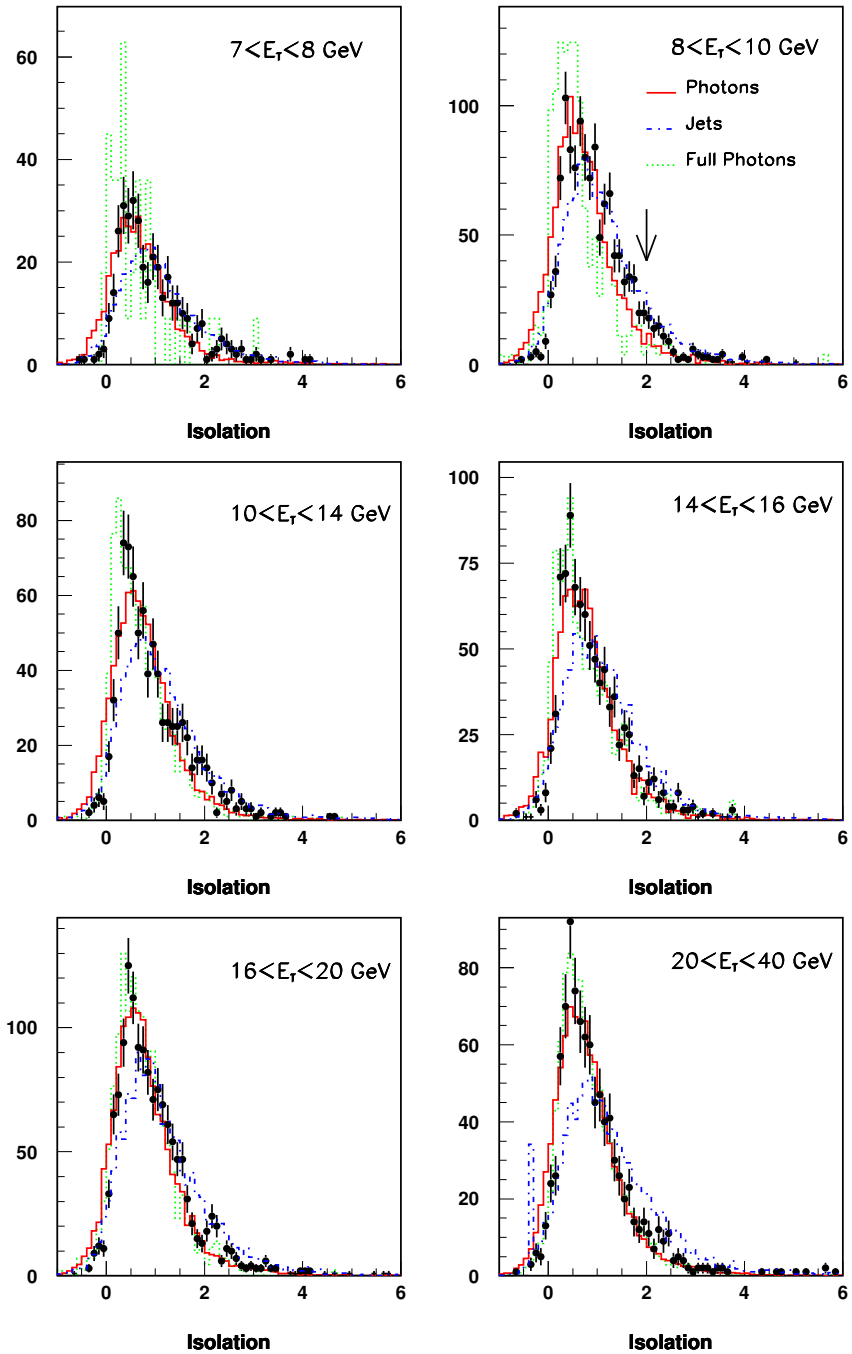

Figure 37: Comparison of Monte Carlo and data for the Isolation in the CC. The key and selection criteria (indicated with an arrow) shown in one E_T region is identical for all E_T regions.

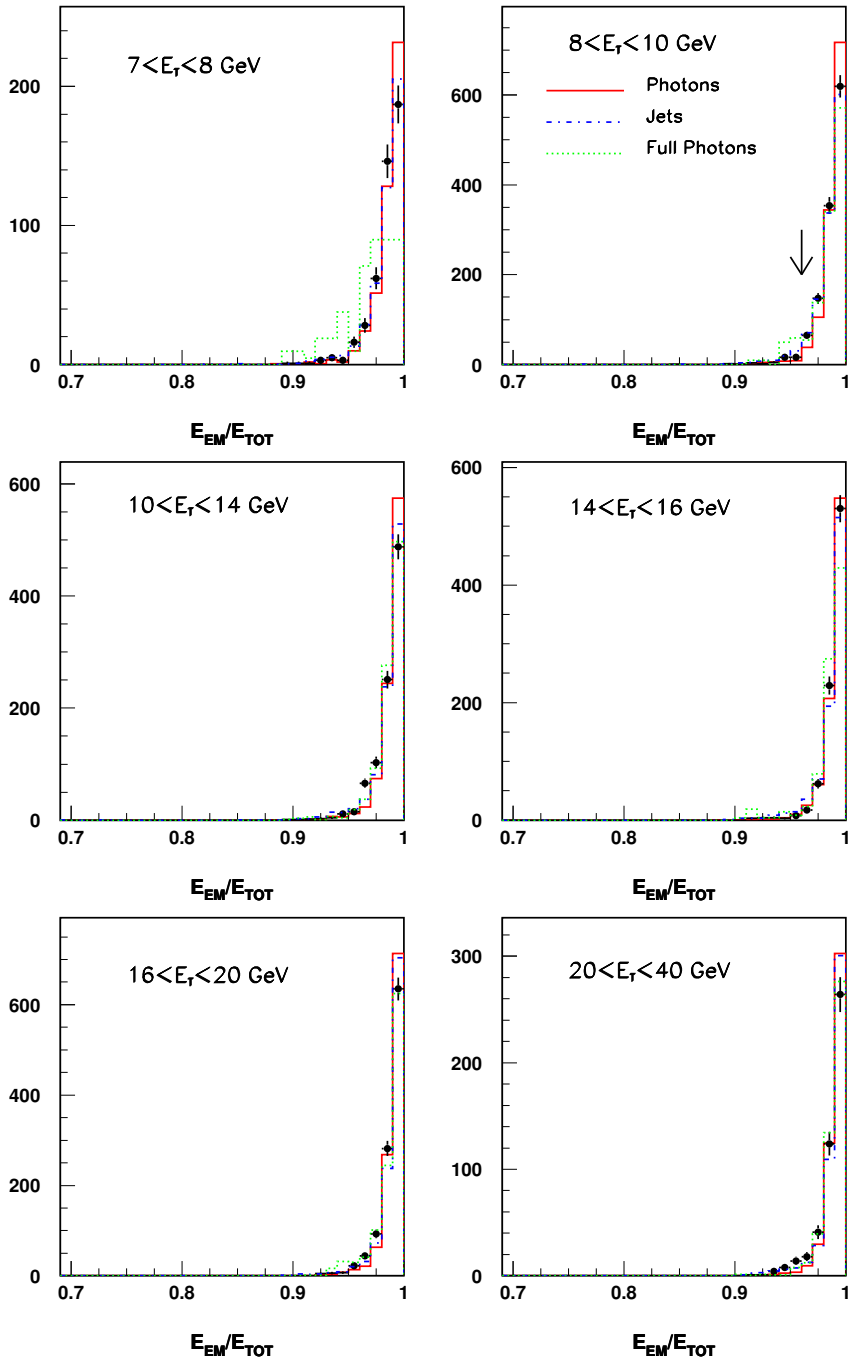

Figure 38: Comparison of Monte Carlo and data for the electromagnetic fraction in the EC. The key and selection criteria (indicated with an arrow) shown in one E_T region is identical for all E_T regions.

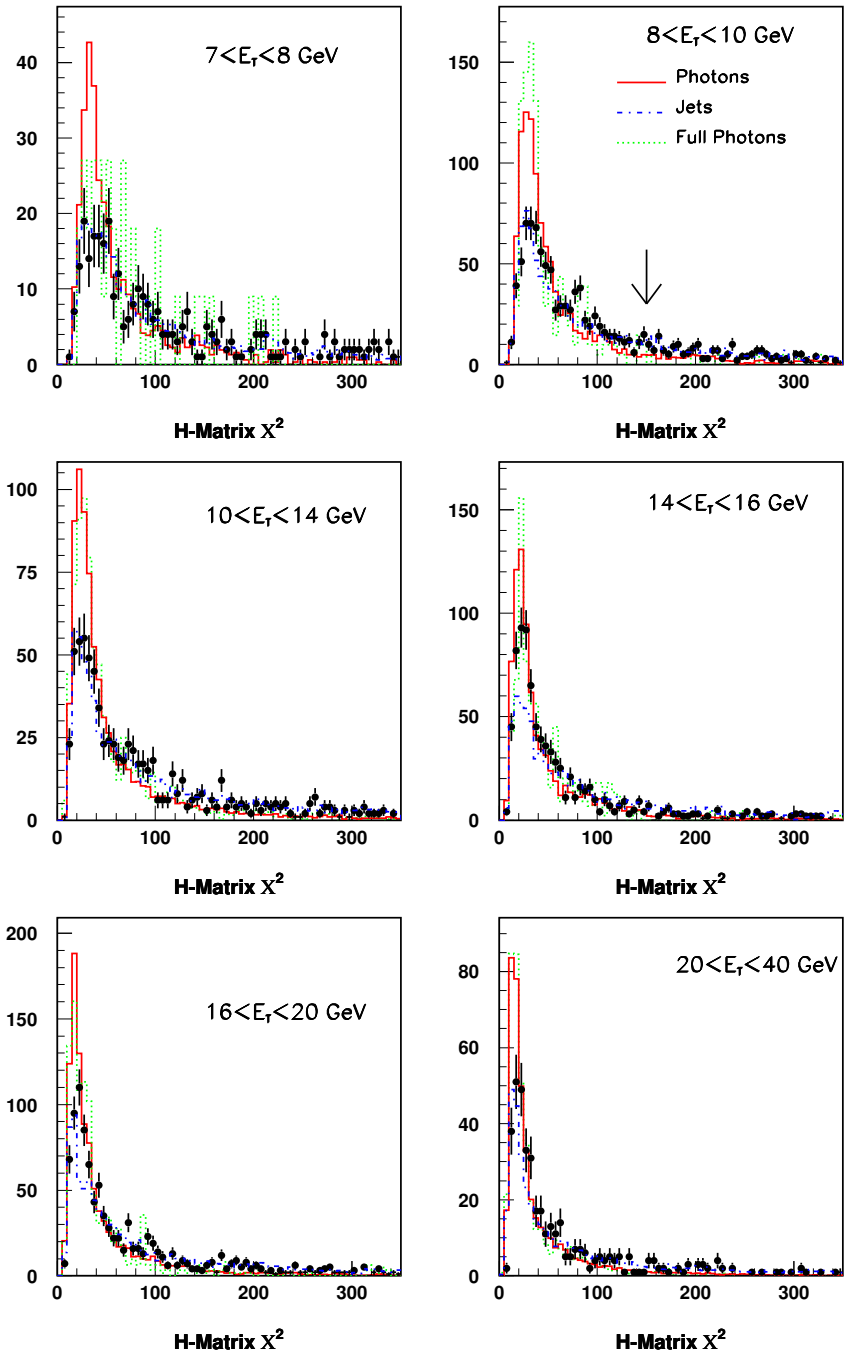

Figure 39: Comparison of Monte Carlo and data for the H-Matrix χ^2 in the EC. The key and selection criteria (indicated with an arrow) shown in one E_T region is identical for all E_T regions.

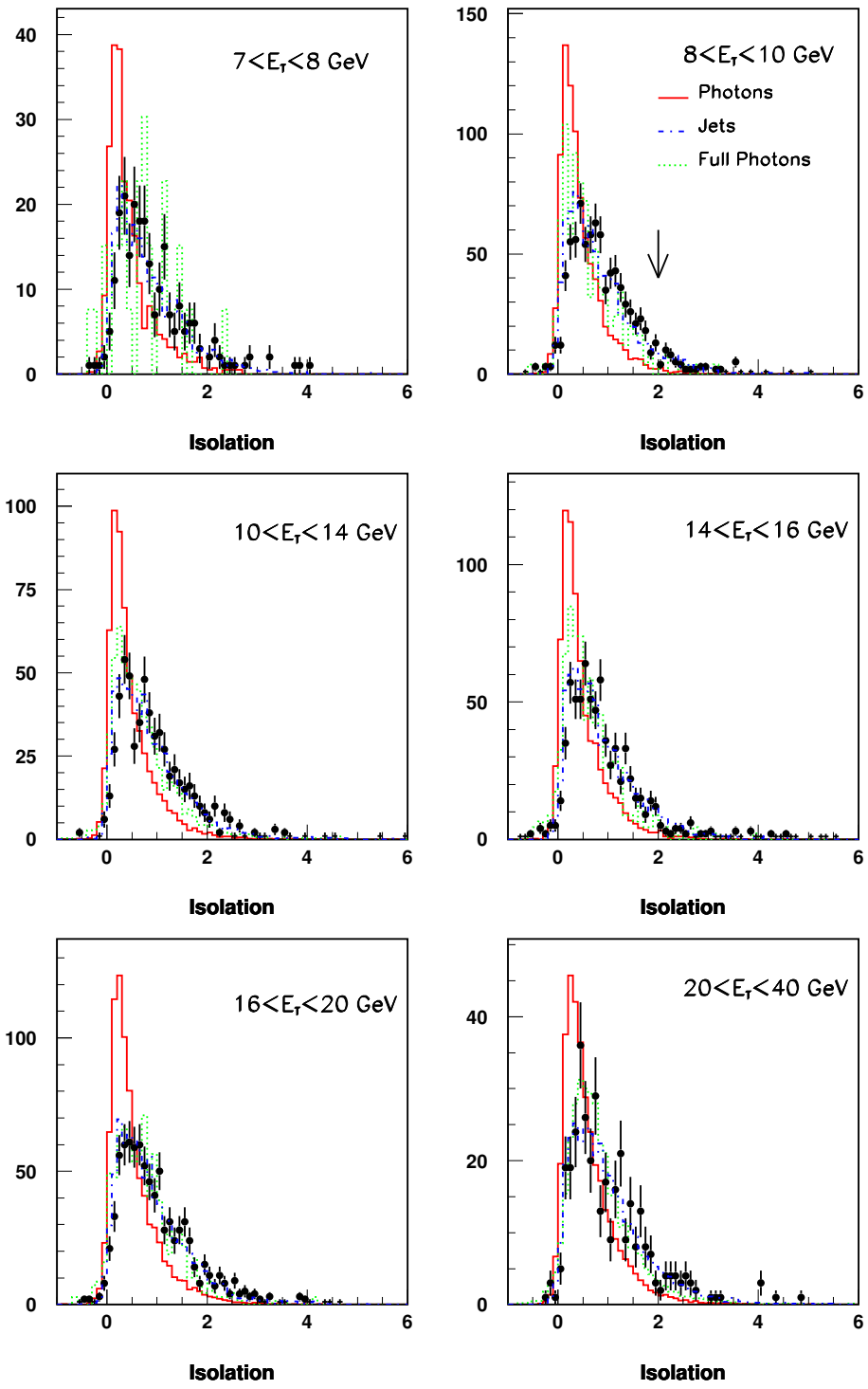

Figure 40: Comparison of Monte Carlo and data for the Isolation in the EC. The key and selection criteria (indicated with an arrow) shown in one E_T region is identical for all E_T regions.

References

[1] "The Isolated Photon Cross Section at $\sqrt{s} = 1.8$," DØ Collaboration, *Phys. Rev. Lett.*, **84**, 2786, 2000.

[2] "The Isolated Photon Cross Section at $\sqrt{s} = 1.8$ TeV Using the Combined Run 1A/B Data Sample
S.L. Linn,DØ Note ♯ 3564, 1999.

[3] "The Isolated Photon Cross Section in the Central and Forward Rapidity Region in $p\bar{p}$ Collisions at $\sqrt{s}$=1.8 TeV".
D0 Collab., Phys. Rev. Letters (77), 5011, (1996)

[4] "The Inclusive Cross Section for Isolated Photons in Run 1a",
S.L. Linn, DØ Note ♯ 2745, 1995.

[5] "Inclusive Direct Photon Production in the Central and Forward Rapidity Regions in Proton-Antiproton Collisions at a Center of Mass Energy of 1800 GeV",
S.A. Jerger, Ph.D. Thesis, Michigan State University, 1997.

[6] "The 630 GeV Isolated Direct Photon Cross Section",
S. Grinstein, R. Piegaia, DØ Note ♯ 3350, 1997.

[7] "Producción de Fotones Directos en Colisiones $p\bar{p}$ a 630 GeV",
S. Grinstein, Tesis de Licenciatura, Universidad de Buenos Aires, 1997.

[8] UA2 Collaboration, J. Alitti *et. al.,* Phys. Lett. **B288** (1992) 386, UA2 Collaboration, J. Alitti *et. al.,* Phys. Lett. **B283** (1991) 554, UA2 Collaboration, Ansari *et. al.,* Z. Phys. **C41** (1988) 395.

[9] CDF Collaboration, F. Abe *et. al.,* Phys. Rev. Lett. **73** (1994) 2662; http://www-cdf.fnal.gov/physics/new/qcd/QCD.html.

[10] S.L. Linn, private communication.

[11] A. Schaffer and S.L. Linn, private communication.

[12] J.F. Owens, Phys. Rev, **D42**, (1990) 61

[13] W. Vogelsang and A. Vogt, Nucl. Phys. **B453**, (1995) 334